Editors' Suggestion

# Spectroscopy and complex-time correlations using minimally entangled typical thermal states

Zhenjiu Wang [1,2,3,*] Paul McClarty,[3,4] Dobromila Dankova,[3] Andreas Honecker [5] and Alexander Wietek [3,†]

[1]*Lanzhou Center for Theoretical Physics, Key Laboratory of Quantum Theory and Applications of MoE, Key Laboratory of Theoretical Physics of Gansu Province, and School of Physical Science and Technology, Lanzhou University, Lanzhou, Gansu 730000, China*

[2]*Arnold Sommerfeld Center for Theoretical Physics, University of Munich, Theresienstr. 37, 80333 Munich, Germany*

[3]*Max Planck Institute for the Physics of Complex Systems, Nöthnitzer Strasse 38, 01187 Dresden, Germany*

[4]*Laboratoire Léon Brillouin, CEA, CNRS, Université Paris-Saclay, CEA Saclay, 91191 Gif-sur-Yvette, France*

[5]*Laboratoire de Physique Théorique et Modélisation, CNRS UMR 8089, CY Cergy Paris Université, 95302 Cergy-Pontoise, France*

(Received 18 June 2024; revised 19 September 2025; accepted 22 September 2025; published 5 January 2026)

Tensor network states have enjoyed great success in capturing aspects of strong correlation physics. However, obtaining dynamical correlators at nonzero temperatures is generically hard even using these methods. Here, we introduce a practical approach to computing such correlators using minimally entangled typical thermal states (METTS). While our primary method directly computes dynamical correlators of physical operators in real time, we propose extensions where correlations are evaluated in the complex-time plane. The imaginary time component bounds the rate of entanglement growth and strongly alleviates the computational difficulty allowing the study of larger system sizes. To extract the physical correlators, one must take the limit of purely real-time evolution. We present two routes for obtaining this information: (i) via an *analytic* correlation function in complex time combined with a stochastic analytic continuation method to obtain the real-time limit and (ii) a *Hermitian* correlation function that asymptotically captures the desired correlation function quantitatively. We show that these numerical techniques capture the finite-temperature dynamics of the Shastry-Sutherland model—a model of interacting spins one-half in two spatial dimensions.

DOI: 10.1103/fc58-w1rr

**CONTENTS**

I. INTRODUCTION 1
II. THE SHASTRY-SUTHERLAND MODEL AND $SrCu_2(BO_3)_2$ 3
III. DYNAMICAL METTS ALGORITHM 4
A. Review of the thermal METTS algorithm 4
B. Dynamical METTS algorithm in real time 4
C. Time evolution using matrix product states 5
D. Spectral analysis and windowing 6
E. Validation by exact diagonalization and DMRG 7
IV. COMPLEX-TIME CORRELATION FUNCTIONS 9
A. Two variants of complex-time correlation functions 9
B. Analytic complex-time correlation functions 10
C. Stochastic analytic continuation 12
V. DISCUSSION AND PERSPECTIVES 13
ACKNOWLEDGMENTS 14
APPENDIX A: HERMITIAN COMPLEX-TIME CORRELATION FUNCTIONS 14
APPENDIX B: GEOMETRY OF THE SIMULATION CYLINDER 16
APPENDIX C: PROJECTION ERROR OF TDVP 16
APPENDIX D: CONVERGENCE IN MPS BOND DIMENSION 17
APPENDIX E: COMPARISON OF WINDOWING FUNCTIONS 17
APPENDIX F: COMPARISON WITH TIME-EVOLUTION FROM EXACT DIAGONALIZATION 18
APPENDIX G: FICTITIOUS TEMPERATURE DEPENDENCE OF STOCHASTIC ANALYTIC CONTINUATION 19
REFERENCES 19

## I. INTRODUCTION

Understanding the macroscopic behavior of quantum materials from microscopic descriptions of strongly interacting particles is one of the great challenges of contemporary physics. Developments in numerical simulations have given us powerful tools to gain insights beyond systems where an analytical treatment is still feasible. While some theoretical models in condensed matter physics are amenable to highly accurate quantum Monte Carlo (QMC) simulations [1], others like frustrated magnets or generic strongly interacting fermion systems present us with the *sign problem* when tackled using QMC [2], limiting the range of parameters and observables that can be studied. Tensor network methods, on the other

*Contact author: wangzj@lzu.edu.cn
†Contact author: awietek@pks.mpg.de

*Published by the American Physical Society under the terms of the Creative Commons Attribution 4.0 International license. Further distribution of this work must maintain attribution to the author(s) and the published article's title, journal citation, and DOI. Open access publication funded by Max Planck Society.*

hand, are not afflicted by a sign problem [3,4]. Instead, these methods face difficulties when dealing with highly entangled states. The most well-known tensor network method is the density matrix renormalization group (DMRG) [5–7], which, in its modern version, is based on matrix-product states (MPS) [8]. Initially proposed as a method to study static properties of ground states, several extensions thereof have enabled the study of static observables at finite temperature [9–18], dynamical spectral functions at zero temperature [19–28], and unitary dynamics in non-equilibrium settings [21,29–35].

To fully build a bridge between microscopic models and their experimental response functions, simulations of dynamical correlators at finite temperature are necessary. This includes dynamical spin structure factors as probed in neutron scattering experiments [36,37], and electronic Green's functions probed in angle-resolved photoemission spectroscopy (ARPES) [38]. Moreover, transport coefficients can be understood within the Kubo linear response formalism. The computation of dynamical response functions at finite temperature in two spatial dimensions, however, still poses significant difficulties for tensor network methods.

A well-known DMRG/MPS-based approach to compute time-dependent correlation functions is to perform real-time evolution. This technique has been applied at zero temperature [21,26,27], but also approaches at finite temperature using purifications have been reported [39–44] as well as an interesting approach to investigate high-temperature transport using dissipation-assisted operator evolution [45]. For alternative approaches to finite-$T$ dynamics, see also Refs. [46,47].

The real-time evolution approach, however, suffers from the fact that the entanglement of generic quantum systems grows unbounded if evolved for long times. In practice, this limits the system size, which can be simulated as well as the resolution of the spectral function which is attained. The computation of real-time correlators is also especially tricky in QMC simulations, where an even more intricate phase problem is encountered. Interestingly, however, much of many-body theory is built on the notion of imaginary-time correlators. While these correlations do not immediately allow for the extraction of dynamical response functions to arbitrary precision at any real frequency, properties like excitation gaps can be reliably estimated [48]. Within the framework of MPS techniques, the computation of imaginary-time evolution does not face the same problem of unbounded entanglement growth. In fact, at asymptotically long times imaginary-time evolution (under mild assumptions) yields the many-body ground state, whose entanglement for most physically relevant systems is expected to be small compared with genuine quantum states with volume-law entanglement. Famously, ground states of locally interacting and gapped systems obey an area law [49,50]. Thus, imaginary-time evolution poses fewer challenges as compared to real-time evolution when applying MPS techniques, which allows one to study larger systems and a wider range of parameters.

In this paper, we introduce an approach to evaluating dynamical spectral functions based on the minimally entangled typical thermal states (METTS) [12–17] technique to simulate systems at nonzero temperature. Moreover, we propose to use a mixed approach where correlators are evaluated in fully complex time, i.e., having both a real-time and imaginary-time component. We present efficient algorithms to obtain the dynamical spectrum of physical operators at nonzero temperature, by computing correlation functions along a certain angle in the complex time plane. Such an approach was originally proposed in Ref. [51] for QMC simulations but has to date not been widely adopted. Recently, however, complex-time correlation functions have been revisited in the context of MPS ground state simulations and applied to quantum impurity models [52,53].

As we will show, complex-time correlation functions can be evaluated using well-known MPS time evolution algorithms such as the time-dependent variational principle (TDVP) [54,55]. Our aim is to combine the advantages of computing imaginary-time correlations and real-time correlations. The imaginary contribution of time evolution dissipates the large entanglement entropy while the real-time part of the correlation function improves the efficiency of obtaining real-frequency spectral function.

We compare two approaches that generalize time evolution to complex times. The first approach generalizes the imaginary time correlator that is well discussed in the QMC community to the complex plane in an analytic way, such that the spectral functions in real frequency can be obtained following a numerical analytical continuation method. In the second approach, we introduce a *Hermitian* complex correlation function, which can be implemented analogously to the real-time correlation function.

This publication also serves as a companion paper to Ref. [56] by the authors, whose goal is to explain the anomalous thermal broadening observed in $SrCu_2(BO_3)_2$ as modeled by the Shastry-Sutherland model [57,58]. At low temperatures, a sharp band of triplon excitations is observed by inelastic neutron scattering experiments [59–61], which rapidly vanishes when the temperature is only raised to a fraction of the gap. From perturbation theory, the triplon gap can be computed as [62]

$$\Delta = J_D\big[1 - (J/J_D)^2 - \tfrac{1}{2}(J/J_D)^3 - \tfrac{1}{8}(J/J_D)^4\big]. \qquad (1)$$

For the coupling ratio $J/J_D = 0.63$ relevant for $SrCu_2(BO_3)_2$ used here, we obtain $\Delta \approx 0.458 J_D$, see also Ref. [56] for more details. On the other hand, the gap in the singlet sector is around $\Delta_S \approx 0.276 J_D$ from our DMRG estimation. To genuinely understand these observations, dynamical spin structure factors at nonzero temperatures need to be evaluated in a controlled way.

The outline of our paper is as follows. We begin with Sec. II introducing the Shastry-Sutherland model we use to benchmark our methods. In Sec. III A, we review the conventional thermal METTS algorithm for simulating static observables at nonzero temperatures. The dynamical METTS algorithm for obtaining spectral function via real-time correlations is introduced in Sec. III B. As both these algorithms are based on efficient matrix-product state time-evolution algorithms, we discuss the time-evolution methods employed in Sec. III C. Details on the Fourier analysis of time-dependent correlation functions are discussed in Sec. III D. To validate our approach, we perform a comparison of the dynamical METTS algorithm to spectral functions obtained via the Lehmann representation using full exact diagonalization and DMRG in Sec. III E.

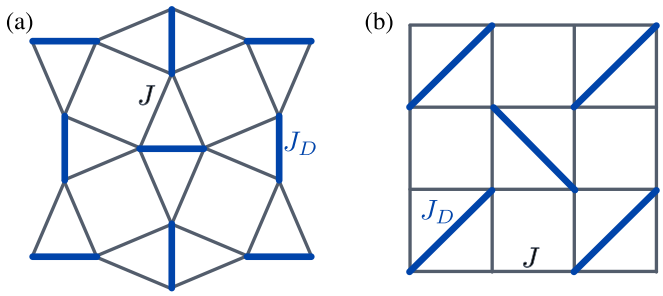



FIG. 1. Sketch of the Shastry-Sutherland lattice geometry. The geometry of copper atoms in $SrCu_2(BO_3)_2$ shown in (a) can be continuously deformed into a square lattice with a $2 \times 2$ unit cell with the additional diagonal bonds as shown in (b). The bold blue bonds are referred to as dimers, $J$ denotes the interdimer couplings marked with gray lines and $J_D$ denotes the intradimer couplings marked with bold blue lines.

In the second part, we discuss how the computational cost from real-time evolution can be eased by performing genuinely complex-time evolution. In Sec. IV A, we introduce two definitions of complex-time correlation functions. One of these, that we call the *analytic* correlation function is an interpolation between the real-time correlation function and the imaginary-time Matsubara Green's functions often employed in many-body physics. We discuss an efficient algorithm evaluating this correlation function using METTS in Sec. IV B. From these correlation functions, the real-time spectral function can be obtained via analytic continuation. We describe our approach employing stochastic analytic continuation in Sec. IV C. We call the second complex-time correlation that we introduce in Sec. IV A the *Hermitian* correlation function. This correlation function is analyzed further in Appendix A, where we show that this correlation can be efficiently evaluated with bounded entanglement.

Finally, we give a summary and perspective in Sec. V. Several appendices provide further technical details complementing the results of the main text.

## II. THE SHASTRY-SUTHERLAND MODEL AND $SrCu_2(BO_3)_2$

The Shastry-Sutherland model [57,58] is chosen to showcase and benchmark our numerical method. The model is given by

$$H = J_D \sum_{\langle i,j \rangle} \boldsymbol{S}_i \cdot \boldsymbol{S}_j + J \sum_{\langle\langle i,j \rangle\rangle} \boldsymbol{S}_i \cdot \boldsymbol{S}_j. \tag{2}$$

where $\boldsymbol{S}_i = (S_i^x, S_i^y, S_i^z)$ denotes the spin-1/2 operators, $J_D$ denotes the intradimer coupling and $J$ denotes the interdimer coupling on the Shastry-Sutherland lattice, see Fig. 1.

The Shastry-Sutherland model [57] provides a classic instance of magnetic frustration in two dimensions. The magnetic moments interact via Heisenberg exchange couplings on bonds organized into triangular units (Fig. 1). When $J = 0$, the lattice breaks up into pairs of interacting spins so that the ground state is a tiling of singlets on the $J_D$ bonds and the elementary excitations are decoupled triplets. Remarkably, the singlet tiling is an exact eigenstate of the fully interacting model (finite $J$) and is the ground state for $J/J_D \lesssim 0.65$. In this paper, we focus on this regime of the model which is also relevant to the material $SrCu_2(BO_3)_2$ [58,63]. In the material, the magnetic copper ions are organized into essentially decoupled layers each forming a Shastry-Sutherland lattice with couplings well approximated by $J/J_D \approx 0.63$ [58,64,65]. The singlet ground state of materials described by the model has been verified experimentally. We are interested in the dynamics of the model that has also been studied extensively. The decoupled triplets at $J = 0$ are coupled at finite $J/J_D$ but magnetic frustration almost perfectly localizes these modes leading to an almost flat band of triply degenerate *triplons* that appear in the dynamical spin-spin correlator. At finite temperature, in the material, the triplon modes have been observed to broaden dramatically [59–61,66,67]. It is this feature on which we focus in the following.

We consider cylindrical geometries of length $L$ and width $W$ with periodic boundary conditions in the short $y$ direction and open boundary conditions in the longer $x$ direction. In this work, we focus on width $W = 4$ and $W = 6$ cylinders with length $L = 16$ (compare Appendix B for further details of the cylinder geometry and the corresponding Brillouin zone). A peculiarity when using open boundary conditions for the Shastry-Sutherland model is that there exist spins that are not coupled by any intradimer coupling $J_D$ and only with interdimer couplings $J$. Flipping such a dangling spin would constitute an artificial boundary mode and, therefore, we remove interdimer couplings that couple to these boundary dangling spins.

We are interested in the dynamical spin structure factor given by

$$S^z(\boldsymbol{q}, \omega) = \int_{-\infty}^{\infty} dt\ e^{i\omega t} \langle S^z(-\boldsymbol{q}, t) S^z(\boldsymbol{q}, 0) \rangle, \tag{3}$$

where we set $\hbar = 1$, $S^z(\boldsymbol{q}, t) = e^{iHt} S^z(\boldsymbol{q}) e^{-iHt}$, and

$$S^z(\boldsymbol{q}) = \frac{1}{\sqrt{N}} \sum_{j=1}^{N} e^{i\boldsymbol{q}\cdot\boldsymbol{r}_j} S_j^z, \tag{4}$$

where $\boldsymbol{r}_i$ denotes the position of site $i$ and $N$ denotes the number of lattice sites. The position of the lattice sites $\boldsymbol{r}_i$ as well as the unit cell and basis sites are given by the square lattice geometry shown in Fig. 1(b). The Shastry-Sutherland model features a nearly flat band of triplon excitations, which stretches throughout the entire Brillouin zone. At low temperatures, we expect similar physical phenomena to occur regardless of the exact momentum. In this paper, we focus on two momenta, $\boldsymbol{q} = (\pi, 0)$ and $\boldsymbol{q} = (\pi/2, \pi/2)$ to illustrate the physics, but expect similar behavior at different values of $\boldsymbol{q}$.

To reduce the boundary effects of the cylinder we use a modified definition,

$$\tilde{S}^z(\boldsymbol{q}) = \frac{1}{\sqrt{N}} \sum_{j=1}^{N} w(\boldsymbol{r}_j) e^{i\boldsymbol{q}\cdot\boldsymbol{r}_j} S_j^z, \tag{5}$$

where $w(\boldsymbol{r}) = w(x, y)$ denotes a windowing function. We choose a Tukey window of width $a = 4$ as defined by

$$w(x,y) = \begin{cases} \frac{1}{2}\left\{1 + \cos\left(\frac{\pi}{a}(x-a)\right)\right\} & \text{if } 0 \leqslant x \leqslant a \\ \frac{1}{2}\left\{1 + \cos\left(\frac{\pi}{a}(x-(L-1)+a)\right)\right\} & \text{if } x \geqslant (L-1)-a \\ 1 & \text{otherwise.} \end{cases} \tag{6}$$

Explicitly, for $L = 16$ and $a = 4$, this means

$$\begin{aligned} w(0,y) &= w(L-1,y) = 0, \\ w(1,y) &= w(L-2,y) \approx 0.14644, \\ w(2,y) &= w(L-3,y) = 0.5, \\ w(3,y) &= w(L-4,y) \approx 0.85355, \end{aligned}$$

and $w(x, y) = 1$ else. For notational simplicity, $S(\boldsymbol{q}, \omega)$ will, in the following, refer to the spectral function employing the windowed definition of $\tilde{S}^z(\boldsymbol{q})$ instead of $S^z(\boldsymbol{q})$, whenever cylindrical boundary conditions are used.

## III. DYNAMICAL METTS ALGORITHM

After first reviewing the thermal METTS algorithm, we introduce the dynamical METTS algorithm. We discuss computational details such as the appropriate choice of MPS time evolution algorithms and windowing for Fourier transformation of data simulated up to a finite time. The algorithm is then validated against results from exact diagonalization and DMRG.

### A. Review of the thermal METTS algorithm

The METTS algorithm [12,13] computes thermal expectation values of any operator $\mathcal{O}$ by sampling over expectation values of certain pure states. Generically, we can write a thermal expectation value as

$$\langle \mathcal{O} \rangle_\beta = \frac{1}{\mathcal{Z}} \mathrm{Tr}[e^{-\beta H}\mathcal{O}] \tag{7}$$

$$= \frac{1}{\mathcal{Z}} \sum_i \langle \sigma_i | e^{-\beta H/2} \mathcal{O} e^{-\beta H/2} | \sigma_i \rangle \tag{8}$$

$$= \frac{1}{\mathcal{Z}} \sum_i p_i \langle \psi_i | \mathcal{O} | \psi_i \rangle, \tag{9}$$

where $\beta = 1/(k_\mathrm{B}T)$ (henceforth $k_\mathrm{B} = 1$) denotes the inverse temperature, $\mathcal{Z} = \mathrm{Tr}[e^{-\beta H}]$ the partition function, and $\langle \ldots \rangle_\beta = \frac{1}{\mathcal{Z}} \mathrm{Tr}[e^{-\beta H} \ldots]$ denotes a thermal expectation value. The sum is performed over the computational basis of product states,

$$|\sigma_i\rangle = \left|\sigma_i^1\right\rangle \left|\sigma_i^2\right\rangle \cdots \left|\sigma_i^N\right\rangle, \tag{10}$$

and we define the METTS state,

$$|\psi_i\rangle = \frac{1}{\sqrt{p_i}} e^{-\beta H/2} |\sigma_i\rangle, \tag{11}$$

where $p_i = \langle \sigma_i | e^{-\beta H} | \sigma_i \rangle \geqslant 0$ is a (non-negative) weight. Notice that the partition function can also be written as $\mathcal{Z} = \sum_i p_i$. The METTS states are normalized, i.e., $|\langle \psi_i | \psi_i \rangle|^2 = 1$. To sample the METTS states $|\psi_i\rangle$ with probability $p_i/\mathcal{Z}$, a Markov chain is constructed where the transition probability is given by

$$T_{i\to j} = |\langle \psi_i | \sigma_j \rangle|^2. \tag{12}$$

The original works on METTS [12,13] proved that this transition probability fulfills the detailed balance conditions,

$$p_i T_{i\to j} = p_j T_{j\to i}, \tag{13}$$

and, therefore, the stationary distribution of this Markov chain is given by the probabilities $p_i$. As a Markov chain Monte Carlo simulation, thermalization and autocorrelation effects have to be taken into account to estimate averages and standard errors. In the following, we denote by $R$ the number of random METTS states sampled. In our calculations, we choose $R = 100$ because of our computational budget, from which we obtain error estimates by analyzing thermalization and autocorrelation times as in standard error analysis of Markov chain Monte Carlo methods. The METTS algorithm is particularly well suited to tensor network simulations describing states of low entanglement. Because of the fact that we sample with non-negative probabilities $p_i$, the Monte Carlo sampling itself is not accompanied by a *sign problem*, as often encountered in QMC simulations. The computational complexity is rather transferred to the entanglement of the METTS states $|\psi_i\rangle$.

### B. Dynamical METTS algorithm in real time

To study dynamical structure factors, we are interested in the *conventional* time-dependent correlation function $\mathcal{C}_{AB}(t)$ given by

$$\mathcal{C}_{AB}(t) = \langle A(t)B \rangle_\beta = \langle e^{iHt} A e^{-iHt} B \rangle_\beta, \tag{14}$$

where $A$ and $B$ denote observables subject to investigation. For the dynamical spin structure factor considered in this work, we choose

$$A^\dagger = B = S^z(\boldsymbol{q}), \tag{15}$$

as defined in Eqs. (4) and (5). A dynamical spectral function is then given as the Fourier transform,

$$\mathcal{C}_{AB}(\omega) = \int_{-\infty}^{\infty} dt\; e^{i\omega t} \mathcal{C}_{AB}(t). \tag{16}$$

We expand the corresponding expectation values in the basis of METTS states,

$$\mathcal{C}_{AB}(t) = \frac{1}{\mathcal{Z}} \sum_i p_i \langle \psi_i | e^{iHt} A e^{-iHt} B | \psi_i \rangle, \tag{17}$$

and define the states,

$$|v_i(t)\rangle = e^{-iHt} B |\psi_i\rangle, \tag{18}$$

$$|w_i(t)\rangle = e^{-iHt} |\psi_i\rangle. \tag{19}$$

Notice, while the state $|w_i(t)\rangle$ is normalized, we generically have

$$\langle v_i(t) | v_i(t) \rangle = \text{constant} \neq 1. \tag{20}$$

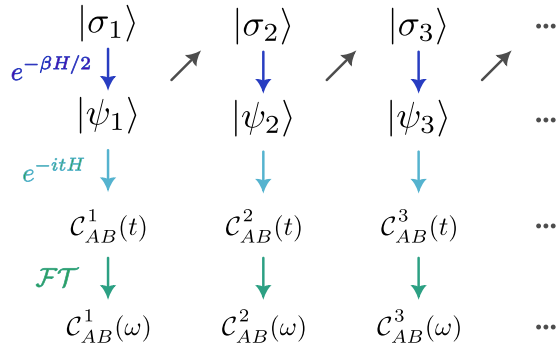



FIG. 2. Illustration of the dynamical METTS algorithm. A sequence of product states $|\sigma_i\rangle$ and METTS $|\psi_i\rangle$ is sampled according to the thermal METTS algorithm. For every METTS the time-dependent correlation function $\mathcal{C}^i_{AB}(t)$ as in Eq. (21) is computed. Product states $|\sigma_{i+1}\rangle$ are sampled with transition probability $T_{i\to i+1} = |\langle\psi_i|\sigma_{i+1}\rangle|$. From the individual METTS correlation functions $\mathcal{C}^i_{AB}(t)$ the spectral function $\mathcal{C}_{AB}(\omega)$ is computed via a Fourier transform and subsequent averaging.

We introduce the time-dependent correlation function of an individual METTS state as

$$\mathcal{C}^i_{AB}(t) \equiv \langle\psi_i|e^{iHt}Ae^{-iHt}B|\psi_i\rangle \tag{21}$$

$$= \langle w_i(t)|A|v_i(t)\rangle. \tag{22}$$

Hence, the time-dependent correlation function and the dynamical spectral function are expressed as

$$\mathcal{C}_{AB}(t) = \frac{1}{\mathcal{Z}}\sum_i p_i\mathcal{C}^i_{AB}(t), \tag{23}$$

$$\mathcal{C}_{AB}(\omega) = \frac{1}{\mathcal{Z}}\sum_i p_i\mathcal{C}^i_{AB}(\omega), \tag{24}$$

where

$$\mathcal{C}^i_{AB}(\omega) = \int_{-\infty}^{\infty} dt\; e^{i\omega t}\mathcal{C}^i_{AB}(t). \tag{25}$$

This suggests the following algorithm to compute dynamical correlation functions $\mathcal{C}^i_{AB}(t)$ and $\mathcal{C}^i_{AB}(\omega)$. We sample METTS states $|\psi_i\rangle$ by sampling from the Markov chain with transition probability $T_{i\to j} = |\langle\psi_i|\sigma_j\rangle|^2$, just as in the thermal METTS algorithm. For every METTS state $|\psi_i\rangle$, we compute $|v_i(0)\rangle = B|\psi_i\rangle$ and set $|w_i(0)\rangle = |\psi_i\rangle$ at the beginning.

The next step is to perform a real-time evolution to compute $|v_i(t)\rangle$ and $|w_i(t)\rangle$ as in Eqs. (18) and (19). Notice that the METTS states $|\psi_i\rangle$ are not eigenstates of the Hamiltonian $H$, such that the time-evolved states $|v_i(t)\rangle$ and $|w_i(t)\rangle$ have to be explicitly computed. Naturally, this time evolution can only be carried out until a maximum time $\Omega$. Measurements of $\mathcal{C}^i_{AB}(t)$ are only performed at discrete time steps that are multiples of an elementary step size $\delta_t$.

For convenience, we introduce the shorthand notations,

$$C(t) = C_{AB}(t), \quad C(\omega) = C_{AB}(\omega), \tag{26}$$

$$C^i(t) = C^i_{AB}(t), \quad C^i(\omega) = C^i_{AB}(\omega). \tag{27}$$

The algorithm laid out above is summarized in Algorithm 1, and illustrated graphically in Fig. 2. Using the Shastry-Sutherland model as a concrete example, we show the

ALGORITHM 1. Dynamical METTS for correlators $\mathcal{C}(t)$.

Choose a random initial product state $|\sigma_1\rangle = |\sigma_1^1\rangle\cdots|\sigma_1^N\rangle$
**for** $i = 1, \ldots, R$ **do**
  Compute the METTS state $|\psi_i\rangle = \frac{1}{\sqrt{p_i}}e^{-\beta H/2}|\sigma_i\rangle$
  Compute $|v_i(0)\rangle = B|\psi_i\rangle$ and set $|w_i(0)\rangle = |\psi_i\rangle$
  Set $t = 0$
  **while** $t \leqslant \Omega$ **do**
    Compute $\mathcal{C}^i(t) = \langle w_i(t)|A|v_i(t)\rangle$
    Compute $|v_i(t+\delta t)\rangle = e^{-iH\delta t}|v_i(t)\rangle$
    Compute $|w_i(t+\delta t)\rangle = e^{-iH\delta t}|w_i(t)\rangle$
    $t \to t + \delta t$
  **end while**
  Store correlator $\mathcal{C}^i(t)$ to disk
  Pick product state $|\sigma_{i+1}\rangle$ with probability $|\langle\psi_i|\sigma_{i+1}\rangle|^2$
**end for**

corresponding correlation function $\mathcal{C}^i_{AB}(t)$ and $\mathcal{C}^i_{AB}(\omega)$ for several sampled METTS states as well as their average value in Fig. 3. At the given temperature $T/J_D = 0.1$, we observe a "bunching" of correlation functions $\mathcal{C}^i_{AB}(t)$ around the $T = 0$ correlation function whereas several other random realizations disperse, illustrating the effect of thermal fluctuations. This behavior is specific to the Shastry-Sutherland model, which exhibits a gap $\Delta_S$ to the lowest excited (singlet) state, estimated to be of size $\Delta_S \approx 0.276J_D$ from DMRG for the $16 \times 4$ system, as mentioned below Eq. (1).

The real-time approach of measuring spectral functions at finite temperature is rigorous in the limit of long times and sufficient sampling of METTS states $|\psi_i\rangle$. However, a limitation of this algorithm is naturally the unbounded growth of entanglement in real-time evolution. In particular, at higher temperatures entanglement growth can hinder accurate calculations. As shown in Fig. 6 below, the bipartite entanglement entropy $S_{\text{vN}}$ of time evolution based on METTS states of the Shastry-Sutherland model at $T/J_D = 0.2$ grows much more quickly on average than the one at $T/J_D = 0.1$. Meanwhile, pronounced fluctuations of the entropy after time evolution exist among various sampled METTS states.

In the limit of infinitely long simulation time $\Omega \to \infty$ and infinitely accurate calculations of the entangled states $|\psi_i\rangle$, $|v_i(t)\rangle$, and $|w_i(t)\rangle$, this algorithm is exact assuming ergodicity of the METTS Markov chain. A finite-time horizon $\Omega$ introduces an artificial broadening to the spectral function on the order of $\propto 1/\Omega$. The accuracy in computing time evolutions of MPS states can be well controlled by modern algorithms described in the next section.

### C. Time evolution using matrix product states

The key computational bottlenecks in the thermal as well as the dynamical METTS algorithm are the computation of the imaginary-time evolution of the product states $|\sigma_i\rangle$ and the real-time evolutions $|v_i(t)\rangle$ and $|w_i(t)\rangle$ of the METTS state $|\psi_i\rangle$. Time-evolution techniques for matrix-product states have received a considerable amount of attention over the years, resulting in several practical methods that are in common use. In a recent review [68], these methods have been thoroughly compared in various test scenarios. These

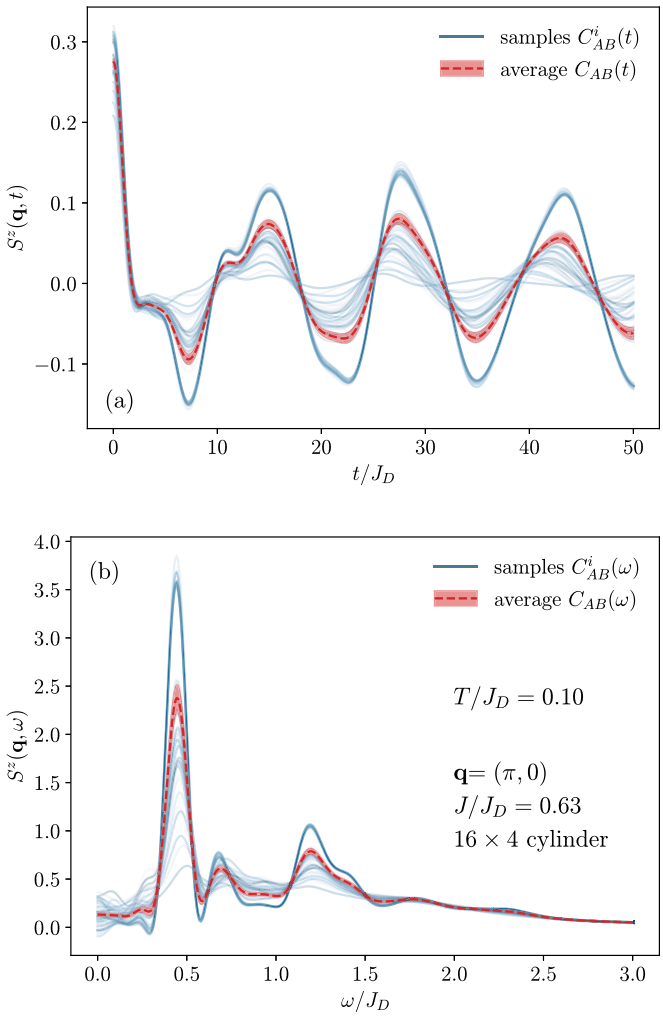



FIG. 3. Exemplary METTS samples (blue lines) of (a) the correlation functions $\mathcal{C}^i_{AB}(t)$ and (b) the spectral functions $\mathcal{C}^i_{AB}(\omega)$ of the Shastry-Sutherland model on a $16 \times 4$ cylinder for $J/J_D = 0.63$ and $T/J_D = 0.1$. We investigate the spin correlations and structure factors with $A^\dagger = B = S^z(\boldsymbol{q})$ as in Eqs. (4) and (5) with $\boldsymbol{q} = (\pi, 0)$. The estimated averages $\mathcal{C}_{AB}(t)$ and $\mathcal{C}_{AB}(\omega)$ with a statistical error estimate from $R = 100$ samples are shown as the red line with the shaded light red region.

thorough comparisons suggest that the time-dependent variational principle (TDVP) for MPS [54,55] often performs optimally, even though other approaches like the WII method [69] can perform equally well.

Similarly to DMRG, the TDVP method can be performed in a single-site (1TDVP) and in a two-site version (2TDVP). While the 1TDVP method conserves energy exactly when performing a real-time evolution and is faster than 2TDVP, it does not allow the bond dimension to be increased without further extensions. 2TDVP, on the other hand, allows the MPS bond dimension to increase during the evolution. Both TDVP methods come with two control parameters. The first one is the time step $\tau$, which can be chosen to be remarkably large while only incurring a small error. In Ref. [14], a detailed study was performed of the accuracy of TDVP depending on the time step size $\tau$. There, a time-step size between $\tau = 0.1, \ldots, 0.2$ in units of the hopping amplitude $t$ of the Hubbard model was found to be optimal. The second control parameter is the cutoff $\varepsilon$, which is the analog of the DMRG truncation error which, here, is chosen to be $10^{-6}$. Interestingly, TDVP does not become more accurate in the limit $\tau \to 0$, as then more truncations necessarily lead to an increased overall error.

When performing long real-time evolutions, we use 2TDVP to increase the MPS bond dimension until a maximal bond dimension $\chi_{\max}$ is encountered. Thereafter, 1TDVP is employed to further time-evolve the MPS. Results are then studied as a function of $\chi_{\max}$ to investigate convergence. A peculiarity of the TDVP algorithm is that upon evolving states with small bond dimensions (e.g., product states), a so-called projection error is encountered [68]. To avoid this error, the initial-time evolution for the thermal METTS states should be performed by a different method with high accuracy. For this purpose, the time-evolving block decimation [70] algorithm has been applied previously [14]. However, more recently a basis extension technique for 1TDVP has been proposed [71], which can be applied easily without necessitating a Trotterization with possible swap gates. In our specific example, at very low temperatures, the projection error leads to a potential issue when evaluating the *analytic* correlation function away from the real-time axis. This is because of the low entanglement property of the ground state of the Shastry-Sutherland model, which we discuss in Appendix C. This issue is specific to the dimer-product ground state of the Shastry-Sutherland model and is not expected to occur in general for more entangled ground states. We validated simulations by confirming convergence in the bond dimension, cf. Fig. 16 in Appendix D. Our implementation is based on the ITensor library [72] and the TDVP package of ITensor [73].

The scaling of the method is determined by the maximal MPS bond dimension $\chi$, which needs to be simulated and the matrix-product operator bond dimension $D$ which typically remains finite. To perform the METTS sampling as well as the time evolution of METTS states, the TDVP time-evolution method has the same scaling as DMRG, which is $\mathcal{O}(\chi^3 D + \chi^2 D^2)$.

### D. Spectral analysis and windowing

Evaluating the METTS spectral functions $\mathcal{C}^i(\omega)$ via the Fourier transform Eq. (25) cannot be done exactly as we are only provided with data for $\mathcal{C}^i(t)$ at discrete times,

$$t = 0,\ \delta_t,\ 2\delta_t,\ \ldots,\ (S-1)\delta_t,\ S\delta_t (= \Omega). \tag{28}$$

In our simulations, we found that a thorough treatment of the Fourier transform is crucial to arrive at accurate spectral functions. A naive discrete Fourier transform of the form

$$\mathcal{C}^i(\omega) \approx \delta_t \sum_{k=-S}^{S} e^{-i\omega k\delta_t} \mathcal{C}^i(k\delta_t), \tag{29}$$

leads to artificial spectral content because of the abrupt end of the signal and cannot be used for accurate measurements of the spectral function. Instead, we employ a windowing function $w(k)$ to consider the windowed Fourier

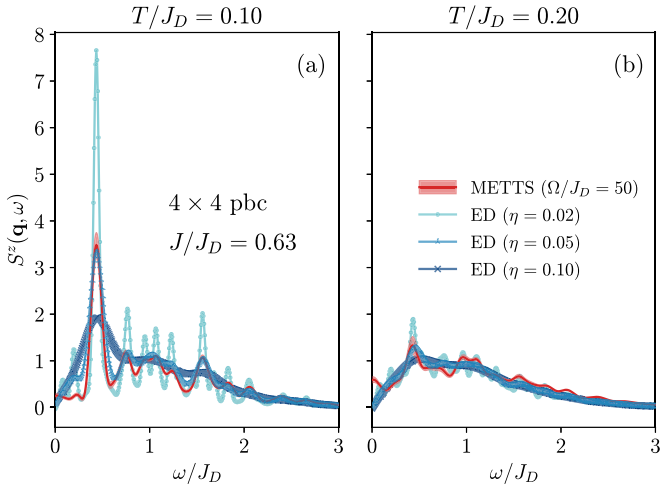



FIG. 4. Comparison of results from dynamical METTS to the spectral function from exact diagonalization on a $4 \times 4$ lattice with fully periodic boundary conditions at $J/J_D = 0.63$ and $\boldsymbol{q} = (\pi/2, \pi/2)$ for temperatures $T/J_D = 0.1$ (a) and $T/J_D = 0.2$ (b). As the exact spectral function from ED is a sum of delta functions, we show Gaussian broadenings for widths $\eta = 0.02, 0.05, 0.10$. For the dynamical METTS, we used $R = 100$ samples with a real-time evolution up to $\Omega/J_D = 50$. We observe close agreement between the METTS results and the ED results at Gaussian broadening $\eta = 0.05$.

transform [74],

$$\mathcal{C}^i(\omega) \approx \delta_t \sum_{k=-S}^{S} e^{-i\omega k\delta_t} \mathcal{C}^i(k\delta_t) w(k). \tag{30}$$

In the context of DMRG simulations of spectral functions at zero temperature, the use of several distinct windowing functions has been reported, including Parzen windows [39] and Gaussian windows [28]. Here, we find that a Hann window of the form

$$w(k) = 0.5 + 0.5 \cos\left(\frac{\pi k}{S}\right), \tag{31}$$

for $k = 0, \ldots, S$ yields the most accurate results when compared to exact time-evolution data in Fig. 4. Hence, we adopt the Hann window as the windowing function in all our subsequent simulations.

Introducing a windowing function reduces the integrated spectral weight. This reduction is commonly remedied by multiplying with a window correction factor [74]. We opt for the so-called energy correction,

$$\Gamma = \sqrt{\frac{1}{2S+1} \sum_{k=-S}^{S} w(k)^2}, \tag{32}$$

conserving the total integrated spectral weight. The estimator for the correct infinite-time Fourier transform is given by

$$\tilde{\mathcal{C}}^i(\omega) = \frac{1}{\Gamma} \mathcal{C}^i(\omega). \tag{33}$$

In the following, we will use the notation $\mathcal{C}^i(\omega)$ implicitly for the energy-corrected spectral function $\tilde{\mathcal{C}}^i(\omega)$.

### E. Validation by exact diagonalization and DMRG

To demonstrate the accuracy of our method, we start by comparing to data on a $4 \times 4$ simulation cluster with periodic boundary conditions, where exact diagonalization (ED) can be straightforwardly performed. In ED, we consider the Lehmann representation of the dynamical spectral function,

$$S^z(\boldsymbol{q}, \omega) = \frac{2\pi}{\mathcal{Z}} \sum_{n,m} e^{-\beta E_n} |\langle m|S^z(\boldsymbol{q})|n\rangle|^2 \delta(\omega - (E_n - E_m)), \tag{34}$$

where $|n\rangle$ and $|m\rangle$ denotes an eigenbasis with corresponding eigenvalues $E_n$ and $E_m$ of the Hamiltonian and $\delta$ denotes the Dirac delta function. The eigenvalues and eigenvectors are computed by a full diagonalization of the Hamiltonian matrix. Hence, both the positions of the poles $(\varepsilon_n - \varepsilon_m)$ as well as the weights are computed with machine precision. To analyze and compare the ED spectral function, it is customary to introduce a broadening of the spectral function by replacing the set of Dirac delta peaks with, e.g., narrow Gaussian functions of width $\eta$,

$$\delta(\omega - p) \longrightarrow \frac{1}{\eta\sqrt{2\pi}} \exp\left[-\frac{(\omega - p)^2}{2\eta^2}\right]. \tag{35}$$

A crucial difference to the proposed METTS method is the fact that the poles and weights are computed exactly and no time evolution is performed. *A priori*, it is not clear which precision can be expected when only simulating up to a maximal time $\Omega$ and also when only having access to the time-dependent correlator at discrete time steps that are a multiple of $\delta t$. Moreover, it is also not obvious what statistical error we can expect from sampling a finite number of METTS states.

To address these questions, we show results from ED as well as dynamical METTS simulations in Fig. 4. We focus on the parameter $J/J_D = 0.63$ and $\boldsymbol{q} = (\pi/2, \pi/2)$ and consider two temperatures $T/J_D = 0.10$ in (a) and $T/J_D = 0.20$ (b). We sampled 1000 METTS and performed a time evolution up to a maximal time of $\Omega/J_D = 50$ for every tenth METTS. By only considering a subset of all sampled METTS, we verified that the measurement time series has a negligible autocorrelation time. We also employed measurements in the $S^x$-basis, to further assure vanishing autocorrelation times, see e.g., [13,14]. We employed 2TDVP as the time-evolution algorithm with a cutoff $\varepsilon = 10^{-6}$ without a constraint on the maximal bond dimension $\chi_{\max}$. While a $4 \times 4$ simulation cluster is arguably small, we would like to point out that the employed fully periodic boundary conditions are not without challenge for MPS methods, since long-range interactions are present. Hence, this benchmark also serves as a good first test of the quality of time-evolution algorithms employed to compute the METTS states as well as the real-time evolution. To compute the spectral function, we first find the real-time correlators by applying the matrix-product operator representing $S^z(\boldsymbol{q})$ directly for a specific $\boldsymbol{q}$ in our simulations instead of measuring correlations between pairs of sites. This is done in order to minimize the number of measurements needed, and to allow for statistical self-averaging across the lattice during sampling. To compute the Fourier transform $S(\boldsymbol{q}, \omega)$ to frequency space, we compared different windowing functions

and found the Hann window Eq. (31) to give the most accurate results, cf. Sec. III D and Appendix E. For ED, we compare three different values of the broadening $\eta = 0.02, 0.05, 0.10$.

We report a close agreement between the ED and METTS simulations. While both the Gaussian broadening $\eta$ for the ED data as well as the finite-time horizon $\Omega$ have a broadening effect on the exact spectrum Eq. (34), we observe that even small intricate structures of the spectrum (likely stemming from the small system size) are accurately captured by the METTS algorithm. In particular, the positions of the numerous side peaks are accurately reproduced, as well as the overall spectral amplitude. Choosing $\Omega/J_D = 50$ and applying the windowing procedure as explained in Sec. III D yields a broadening of the spectral function comparable to a Gaussian broadening $\eta \approx 0.05$ in ED. Hence, we conclude that having a finite-time horizon $\Omega$ as well as only a discrete set of measurements with time steps $\delta_t$ only leads to a small broadening of the spectrum. Discrepancies around the $\omega \to 0$ limit stem from the finite-simulation time-horizon $\Omega$, as explained in detail in Appendix F. Moreover, we report that averaging over only $R = 100$ METTS yields a satisfyingly small statistical error indicated by the shaded regions.

We now compare the results from simulations at nonzero temperature with ground-state spectral functions from DMRG. This demonstrates the accuracy of the dynamical METTS algorithm in the limit of low temperatures. Results for spectral functions at different temperatures, including $T = 0$ from DMRG, are shown in Fig. 5. We focus on the $16 \times 4$ cylinder at $J/J_D = 0.63$ and two wave vectors $\boldsymbol{q} = (\pi, 0)$ and $\boldsymbol{q} = (\pi/2, \pi/2)$. Our maximal time horizon for the real-time evolution has been chosen as $\Omega/J_D = 50$. Moreover, we collected $R = 100$ independent METTS states for each temperature and observed that this allows sharp error estimates with a large signal-to-noise ratio, as apparent by the small error bars in Fig. 5. The time evolution has been performed using 2TDVP with maximal bond dimensions $\chi_{\max} = 1000, 1500, 2000$. Comparing different bond dimensions for different seeds leads us to conclude that for this particular system, the sample real-time correlation functions $C^i(t)$ are already well converged at $\chi_{\max} = 1000$. The spectral function from DMRG has similarly been obtained by a single time-evolution up to time $\Omega/J_D = 50$. We observe a structured spectrum, where the dominant peak corresponds to single triplon excitations and secondary and tertiary peaks correspond to multi-triplon excitations of the Shastry-Sutherland model. The good convergence towards the DMRG results for $T \to 0$, where even small features such as secondary and tertiary peaks are well resolved, demonstrates the accuracy of the approach at low temperatures.

A key quantity determining the accuracy of matrix product states is the von Neumann entanglement entropy,

$$\mathcal{S}_{\mathrm{vN}}(\rho, A) = -\mathrm{Tr}[\rho_A \ln(\rho_A)], \tag{36}$$

where the reduced density matrix with respect to a subsystem $A$ is given by $\rho_A = \mathrm{Tr}_B[\rho]$ ($B$ denotes the complement of $A$), ln denotes the natural logarithm, and $\rho$ denotes an arbitrary density matrix. For pure states $|\psi\rangle$, the density matrix is given by

$$\rho(|\psi\rangle) = |\psi\rangle\langle\psi|. \tag{37}$$

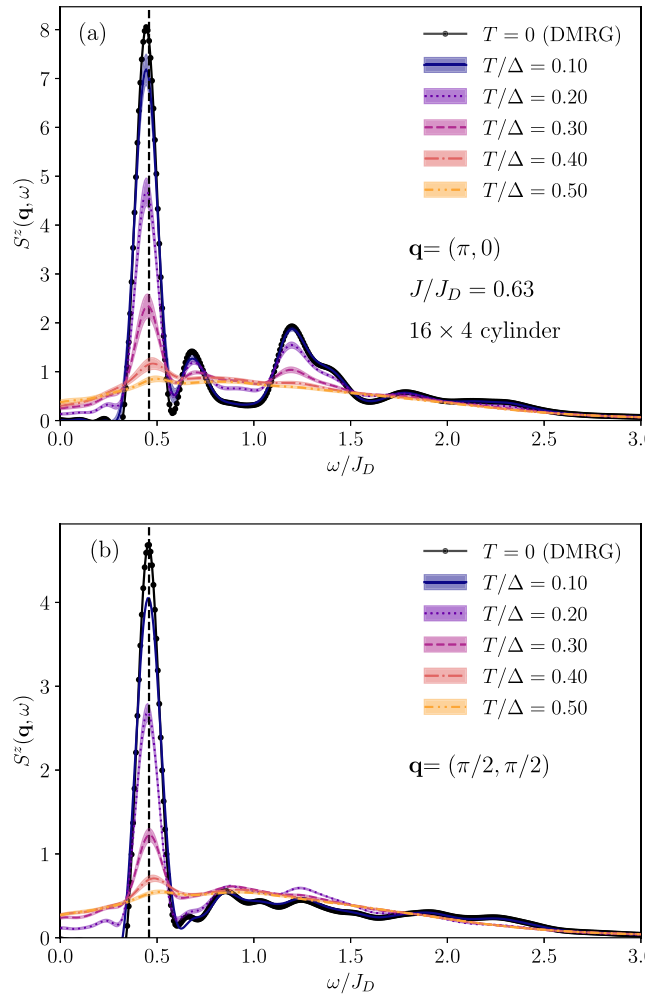



FIG. 5. Dynamical spin structure factor $S^z(\boldsymbol{q}, \omega)$ of the Shastry-Sutherland model at $J/J_D = 0.63$ on a $16 \times 4$ cylinder obtained using the real-time dynamical METTS algorithm at various temperatures in units of the triplon gap $\Delta = 0.458 J_D$. We compare with $S^z(\boldsymbol{q}, \omega)$ at $T = 0$ obtained using DMRG for momenta $\boldsymbol{q} = (\pi, 0)$ (a) and $\boldsymbol{q} = (\pi/2, \pi/2)$ (b). Shaded regions depict the standard error of the estimator obtained from $R = 100$ METTS states with time evolution up to time $\Omega/J_D = 50$. MPS time evolution has been performed using the 2TDVP algorithm with $\chi_{\max} = 2000$. We observe that even small features, as well as secondary and tertiary peaks, are well resolved and converge towards the DMRG result for $T \to 0$.

For any METTS state $|\psi_i\rangle$, the entanglement entropy in the limit $T \to \infty$ is vanishing, as then the METTS state is a product state. In the limit $T \to 0$, the METTS states approach the ground state and its entanglement entropy is naturally bounded. We analyze the behavior of the time-evolved METTS states $|v_i(t)\rangle$ as in Eq. (18) in the dynamical METTS algorithm. Results for the $16 \times 4$ cylinder with $J/J_D = 0.63$ are shown in Fig. 6. The data shown have been obtained using 2TDVP with a maximal bond dimension $\chi_{\max} = 2000$. We observe a significant increase in entanglement entropy for a bipartition in the center of the system over the simulated time horizon. Increasing the temperature also leads to an increase in the entanglement entropy of the time-evolved states $|v_i(t)\rangle$ even though the original METTS states $|\psi_i\rangle$ have lower entan-

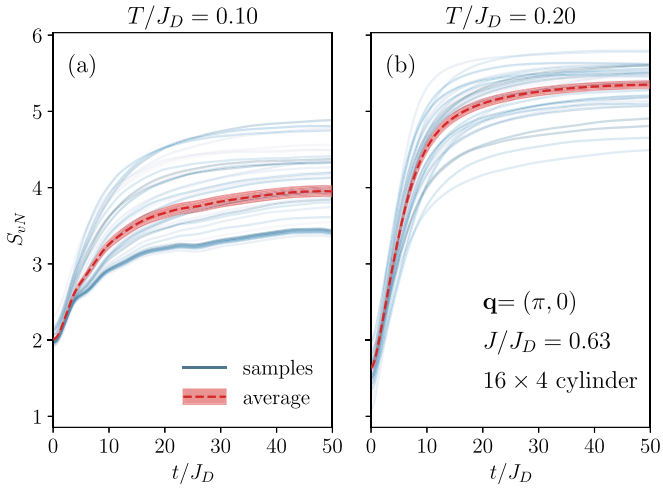



FIG. 6. von Neumann entanglement entropy $S_{\mathrm{vN}}$ of time-evolved METTS states $|v_i(t)\rangle$ from Eq. (18) on the $16 \times 4$ lattice for a bipartition in the center of the lattice. We choose $J/J_D = 0.63$ and $\boldsymbol{q} = (\pi, 0)$. Increasing the temperature from $T/J_D = 0.1$ (a) to $T/J_D = 0.2$ (b) increases the average entanglement entropy, as shown by the red line with the shaded region estimating the statistical error from $R = 100$ samples.

glement at a higher temperature. The behavior of the second kind of auxiliary states $|w_i(t)\rangle$ is similar.

We observe an increase in METTS entanglement upon increasing temperatures. For low temperatures, we expect the METTS to be a superposition of low-energy eigenstates with low entanglement, while higher entanglement at higher temperatures originates from highly entangled states at higher energies of the spectrum.

Even though the growth of entanglement is sizable for this system, the time-dependent correlation functions $C^i(t)$ can still be converged with $\chi_{\max} = 1000, 1500, 2000$ on the width $W = 4$ cylinder, see Fig. 16 below. This changes when considering cylinders of width $W = 6$. There, we found that correlation functions even at a bond dimension $\chi_{\max} = 2000$ can fail to converge for several samples, especially when increasing temperature. For this reason, we introduce, in the next section, the complex-time correlation function as an approach to limit the growth of entanglement.

## IV. COMPLEX-TIME CORRELATION FUNCTIONS

Highly entangled quantum states typically require a large bond dimension to be accurately compressed using a matrix-product state, which limits the system sizes that can reliably be studied. In the present case, we found the width $W = 4$ cylinders to be amenable to the accurate real-time evolution algorithm, whereas $W = 6$ is significantly more challenging and ultimately did not lead to converged results given our current computational resources. The main problem hindering such simulations is the entanglement growth with simulation time if performing real-time evolution, as shown for $W = 4$ in Fig. 6. In the following sections, we discuss how this problem can be ameliorated, by performing complex-time evolution.

### A. Two variants of complex-time correlation functions

Real-time evolution of MPS is computationally expensive as a result of unbounded entanglement growth for generic wave functions. Imaginary-time correlation functions, on the other hand, can be efficiently computed since for imaginary-time $\tau \to \infty$ every wavefunction $|\phi\rangle$ will converge to the ground state $|\psi_0\rangle$ whenever both wave functions have non-vanishing overlap $|\langle\phi|\psi_0\rangle| \neq 0$, i.e.,

$$\lim_{\tau\to\infty} e^{-\tau H}|\phi\rangle \simeq |\psi_0\rangle, \tag{38}$$

where $\simeq$ denotes equivalence up to a phase of the normalized quantum states. In the following, we will parametrize a line through the origin in the complex plane by the angle $\theta$,

$$z = t - i\tau = |z|e^{-i\theta}. \tag{39}$$

The negative sign when defining $\tau$ in Eq. (39) is owed to the fact that we aim to perform imaginary-time evolutions only with negative exponents and this convention simplifies further notation significantly. For real-time evolution, we write a time-dependent correlation function in terms of the time-evolution operator $U(t)$,

$$\mathcal{C}_{AB}(t) = \langle A(t)B\rangle, \quad \text{where} \quad A(t) = U(t)^\dagger A U(t), \tag{40}$$

where $U(t) = \exp(-iHt)$ denotes the unitary time-evolution operator of the time-independent Hamiltonian $H$. $U$ being unitary rests both on the fact that $H$ is Hermitian and on the fact that $t$ is real. Hence, the complex time-evolution operator of the form

$$\mathcal{U}(z) = e^{-iHz}, \tag{41}$$

where $z \in \mathbb{C}$ now denotes a complex time, is generically not a unitary operator for $\mathrm{Im}(z) \neq 0$,

$$\mathcal{U}(z)^{-1} \neq \mathcal{U}(z)^\dagger. \tag{42}$$

There are two natural alternatives when defining complex-time correlation functions,

$$\mathcal{A}_{AB}(z) = \langle \mathcal{U}(z)^{-1} A \mathcal{U}(z) B\rangle_\beta = \langle e^{iHz} A e^{-iHz} B\rangle_\beta, \tag{43}$$

$$\mathcal{H}_{AB}(z) = \langle \mathcal{U}(z)^\dagger A \mathcal{U}(z) B\rangle_\beta = \langle e^{iHz^\star} A e^{-iHz} B\rangle_\beta. \tag{44}$$

Here, we denote by $z^\star = t + i\tau$ the complex conjugate of $z$. $\mathcal{A}(z)$ is an analytical function of $z$ and therefore we will refer to this quantity as the *analytic* correlation function. Moreover, for purely imaginary times this correlation function is given by

$$\mathcal{A}_{AB}(-i\tau) = \langle e^{H\tau} A e^{-H\tau} B\rangle_\beta, \tag{45}$$

which is the well-known imaginary-time correlation function used in the Matsubara formalism.

One notices that evaluating $\langle\psi_i|e^{H\tau}$ from the left-hand side of Eq. (45) necessarily requires a time-evolution process with *positive* time $\tau$. Computing a positive exponential $e^{+\tau H}|\psi_i\rangle$ is numerically highly unstable and prohibits most practical calculations. This is because of the fact that the initial METTS state is a low-energy state. High-energy contributions are truncated during the time evolution but would need to be resolved accurately when performing positive-time evolution, causing severe numerical instabilities. Clearly, this instability issue exists not only for imaginary-time evolution but also for

generic complex time. As we will demonstrate in Sec. IV B, this issue in the evaluation of $\mathcal{A}_{AB}(z)$ can be circumvented within a METTS algorithm in an efficient way.

The Hermitian correlator $\mathcal{H}_{AB}(z)$ as in Eq. (44), on the other hand, has only recently been investigated in the context of MPS and impurity models [53] and has several intriguing properties; these are discussed in Appendix A. We choose the name *Hermitian*, since whenever $A$ is a Hermitian operator, i.e., $A^\dagger = A$, the time-evolved operator $\mathcal{U}(z)^\dagger A \mathcal{U}(z)$ is also Hermitian. This property is shared with the real-time correlation function, but not with the analytic correlation function, where in general $\mathcal{A}_{AB}(z)^\star \neq \mathcal{A}_{BA}(z)$. For convenience, we again introduce the shorthand notations,

$$\mathcal{A}(z) = \mathcal{A}_{AB}(z), \tag{46}$$

$$\mathcal{H}(z) = \mathcal{H}_{AB}(z). \tag{47}$$

There are significant computational advantages in evaluating the time-dependent correlation functions $\mathcal{A}(z)$ and $\mathcal{H}(z)$. In the following Sec. IV B we will discuss the numerical calculation of the analytical correlation function $\mathcal{A}(z)$ in the complex time domain. We then discuss in Sec. IV C how to perform analytic continuation of the resulting complex-time data to the real-time axis. Analytical continuation of the Hermitian correlation function $H(z)$ is less obvious. We therefore relegate discussion of its numerical calculation to Appendix A.

### B. Analytic complex-time correlation functions

We propose an efficient method for evaluating the *analytic* complex-time correlation function $\mathcal{A}(z)$. Its definition as in Eq. (43) is expressed as

$$\begin{aligned}\mathcal{A}(z) &= \langle e^{iHz} A e^{-iHz} B\rangle_\beta \\ &= \frac{1}{\mathcal{Z}} \sum_i p_i \langle \psi_i | e^{izH} A e^{-izH} B | \psi_i\rangle\end{aligned} \tag{48}$$

into the basis of METTS $|\psi_i\rangle$. We choose to evaluate the analytical correlator on the contour $z = |z| e^{-i\theta}$ for

$$|z| \in [0, \Omega], \quad \mathrm{Re}(z) \geqslant 0, \tag{49}$$

where $\Omega$ denotes a final-time horizon. We define

$$\Omega_t = \Omega \cos\theta, \quad \Omega_\tau = \Omega \sin\theta, \quad \Omega_z = \Omega_t - i\Omega_\tau. \tag{50}$$

Thus, the real- and imaginary-time components take values

$$t \in [0, \Omega_t] \subseteq \mathbb{R}, \quad \tau \in [0, \Omega_\tau] \subseteq \mathbb{R}. \tag{51}$$

A naive approach to evaluating $\mathcal{A}(z)$ would be to compute intermediate states,

$$|v_i(z)\rangle = e^{-iHz} B |\psi_i\rangle = e^{-iHt} e^{-\tau H} B |\psi_i\rangle, \tag{52}$$

$$|w_i(z)\rangle = e^{-iHz^\star} |\psi_i\rangle = e^{-iHt} e^{+\tau H} |\psi_i\rangle, \tag{53}$$

with $z = t - i\tau$ similar to the real-time correlation algorithm Algorithm 1.

When restricting our time horizon to $\Omega_\tau = \beta/2$, we can circumvent ever having to compute a positive real exponential in the context of the METTS algorithm. Thus, given that we are only interested in simulating complex times with $\Omega_\tau < \beta/2$, we propose that the analytic correlator can be evaluated in a numerically stable way. This is done by absorbing part of the positive-time evolution into the negative-time evolution performed for the METTS states. Notice that a smaller complex angle $\theta$ allows a longer real-time component $\Omega_t = \Omega \cos\theta$ while still fulfilling $\Omega_\tau = \Omega \sin\theta \leqslant \beta/2$.

The key idea is that the positive imaginary-time evolution can be absorbed by the negative-imaginary time evolution performed when calculating an individual METTS $|\psi_i\rangle$. For this, we rewrite Eq. (48) as

$$\begin{aligned}\mathcal{A}(z) &= \langle e^{izH} A e^{-izH} B\rangle_\beta \\ &= \langle e^{-i\Omega_t H} e^{izH} A e^{-izH} B e^{i\Omega_t H}\rangle_\beta \\ &= \frac{1}{\mathcal{Z}} \sum_i p_i \langle \psi_i | e^{-i\Omega_t H} e^{izH} A e^{-izH} B e^{i\Omega_t H} | \psi_i\rangle \\ &= \frac{1}{\mathcal{Z}} \sum_i p_i \, \mathcal{A}^i(z),\end{aligned} \tag{54}$$

where we defined the sample analytic correlation function as

$$\mathcal{A}^i(z) \equiv \langle \psi_i | e^{-i\Omega_t H} e^{izH} A e^{-izH} B e^{i\Omega_t H} | \psi_i\rangle. \tag{55}$$

Introducing the factor $e^{\pm i\Omega_t H}$ as in Eq. (54) allows to rewrite $\mathcal{A}^i(z)$ in a simple form,

$$\begin{aligned}\mathcal{A}^i(z) &= \langle \psi_i | e^{-i\Omega_t H} e^{izH} A e^{-izH} B e^{i\Omega_t H} | \psi_i\rangle \\ &= \frac{1}{p_i} \langle \sigma_i | e^{-i(\Omega_z - z)H} A e^{-izH} B e^{i\Omega_z^* H} | \sigma_i\rangle.\end{aligned} \tag{56}$$

The analytic correlator $\mathcal{A}(z)$ can then be evaluated without ever having to perform an imaginary-time evolution with positive time $e^{+\tau H}|\psi\rangle$. For actual computations, we discretize the complex time $z$ into $S$ steps with step size $\delta_z = \Omega_z/S$, i.e.,

$$z = 0, \quad \delta_z, \quad 2\delta_z, \ldots, (S-1)\delta_z, \quad S\delta_z (= \Omega_z), \tag{57}$$

where

$$\delta_z = \delta_t - i\delta_\tau = |\delta_z| e^{-i\theta}. \tag{58}$$

The complex contour and the quantities $\Omega_z$, $\Omega_t$, $\Omega_\tau$ for which we evaluate $\mathcal{A}(z)$ are shown in Fig. 7.

For $k = 0, \ldots, S$, we introduce the auxiliary computational states $|\phi_i^k\rangle$ and $|\chi_i^k\rangle$ defined as

$$|\phi_i^k\rangle \equiv \frac{1}{\sqrt{p_i}} e^{ik\delta_z^* H} |\sigma_i\rangle \quad = \frac{1}{\sqrt{p_i}} e^{ik\delta_t H} e^{-k\delta_\tau H} |\sigma_i\rangle, \tag{59}$$

$$|\chi_i^k\rangle \equiv e^{-ik\delta_z H} B |\phi_i^S\rangle \quad = e^{-ik\delta_t H} e^{-k\delta_\tau H} B |\phi_i^S\rangle. \tag{60}$$

Importantly, we see that these states can all be computed by performing a negative imaginary-time evolution, i.e., computing $e^{-\tau H}|\psi\rangle$ for some state $|\psi\rangle$. This insight is the main reason why $\mathcal{A}^i(z)$ can be computed efficiently. Notice that

$$\langle \phi_i^{S-k}| = \frac{1}{\sqrt{p_i}} \langle \sigma_i | e^{-i(\Omega_z - k\delta_z)H}, \tag{61}$$

$$|\phi_i^S\rangle = \frac{1}{\sqrt{p_i}} e^{i\Omega_z^* H} |\sigma_i\rangle. \tag{62}$$

Using a discretized $z = k\delta_z$ we can rewrite Eq. (56) as

$$\mathcal{A}^i(k\delta_z) = \langle \phi_i^{S-k} | A | \chi_i^k\rangle. \tag{63}$$

To evaluate these expectation values for all discretized values of $z = k\delta_z$ ($k = 0, \ldots, S$), we compute the states $|\phi_i^k\rangle$

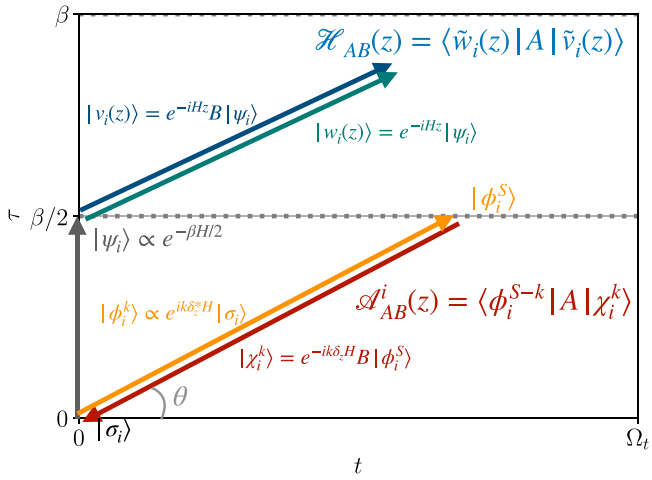



FIG. 7. Sketch of the complex contours on which the analytical correlation function $\mathcal{A}(z)$ and the Hermitian correlation functions $\mathcal{H}(z)$ are evaluated. For the analytical correlation function, the maximal imaginary time is chosen to be $\Omega_\tau = \beta/2$ in order to allow for an efficient and stable numerical algorithm.

for $k = 0, \ldots, S$ successively by complex-time evolution and store all intermediate states to disk for later use. Then, we compute the state $|\chi_i^0\rangle = B|\psi_i^S\rangle$ from which we successively compute $|\chi_i^k\rangle$ for $k = 1, \ldots, S$, and thereby evaluate the desired correlation functions $\mathcal{A}^i(z) = \langle\phi_i^{S-k}|A|\chi_i^k\rangle$. $\mathcal{A}(z)$ is then obtained by averaging over $\mathcal{A}^i(z)$. We summarize the described algorithm in Algorithm 2.

Algorithm 2 is in several aspects similar to Algorithm 1. Both algorithms require computing the METTS $|\psi_i\rangle$ and then time-evolving two further states to compute time-dependent correlators. Moreover, the basic thermal METTS Markov chain is constructed in both cases. A difference in Algorithm 2 is the necessity of storing the auxiliary states $|\phi_i^k\rangle$. On

ALGORITHM 2. Dynamical METTS for analytic correlator $\mathcal{A}(z)$.

Choose a random initial product state $|\sigma_1\rangle = |\sigma_1^1\rangle \cdots |\sigma_1^N\rangle$
**For** $i = 1, \ldots, R$
  Compute $|\psi_i\rangle = \frac{1}{\sqrt{p_i}} e^{-\beta H/2}|\sigma_i\rangle$ and $p_i = \langle\sigma_i|e^{-\beta H}|\sigma_i\rangle$
  Set $|\phi_i^0\rangle = \frac{1}{\sqrt{p_i}}|\sigma_i\rangle$
  **For** $k = 1, \ldots, S$ **do**
    Compute $|\phi_i^k\rangle = e^{i\delta_t H}e^{-\delta_\tau H}|\phi_i^{k-1}\rangle$
    Store $|\phi_i^k\rangle$ to disk for later use
  **end for**
  for $k = 0, \ldots, S$
    **if** $k = 0$ **do**
      Compute $|\chi_i^0\rangle = B|\phi_i^S\rangle$
    **else**
      Compute $|\chi_i^k\rangle = e^{-i\delta_t H}e^{-\delta_\tau H}|\chi_i^{k-1}\rangle$
    **end for**
    Read $|\phi_i^{S-k}\rangle$ from disk
    Evaluate $\mathcal{A}^i(k\delta_z) = \langle\phi_i^{S-k}|A|\chi_i^k\rangle$
  **end for**
  Pick next product state $|\sigma_{i+1}\rangle$ with probability $|\langle\psi_i|\sigma_{i+1}\rangle|^2$
**end for**

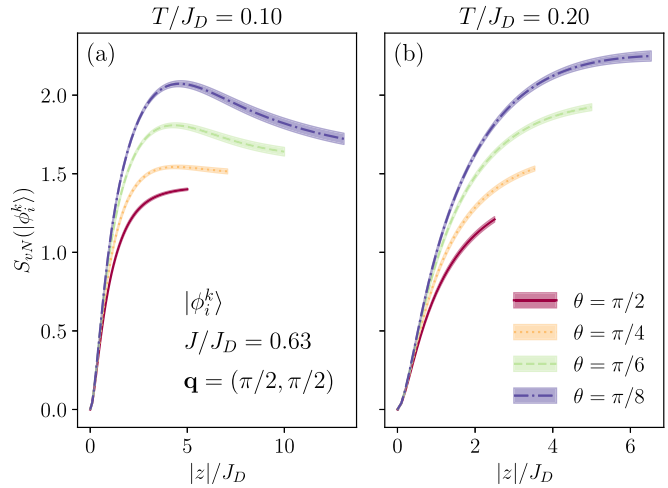



FIG. 8. Average bipartite von Neumann entanglement entropy $S_{\mathrm{vN}}$ of the auxiliary state $|\phi_i^k\rangle$ Eq. (59) for evaluating the analytical correlation function $\mathcal{A}(z)$. We consider the $16 \times 4$ Shastry-Sutherland lattice for different values of the complex angle $\theta$ and $J/J_D = 0.63$ and compare results for temperatures (a) $T/J_D = 0.1$ and (b) $T/J_D = 0.2$. The average is computed from $R = 100$ METTS and the shaded region shows the estimated standard deviation of the mean.

present-day computers, this typically neither imposes severe time nor memory constraints. However, in the limit of small angle $\theta$, the memory requirement can be considerable because of the large number of discrete time steps and requires corresponding storage capacities.

The key quantity determining the efficiency of the algorithm is the bipartite von Neumann entanglement entropy $S_{\mathrm{vN}}$ as in Eq. (36) of the MPS $|\phi_i^k\rangle$ and $|\chi_i^k\rangle$, shown in Figs. 8 and 9, respectively. The entanglement is considered for a bipartition at the center of the system. We evaluated the analytic correlator for the dynamical spin structure factor $S^z(\boldsymbol{q}, \omega)$ as in Eq. (3) for the $16 \times 4$ Shastry-Sutherland model at $J/J_D = 0.63$ at temperatures $T/J_D = 0.1$ and $T/J_D = 0.2$.

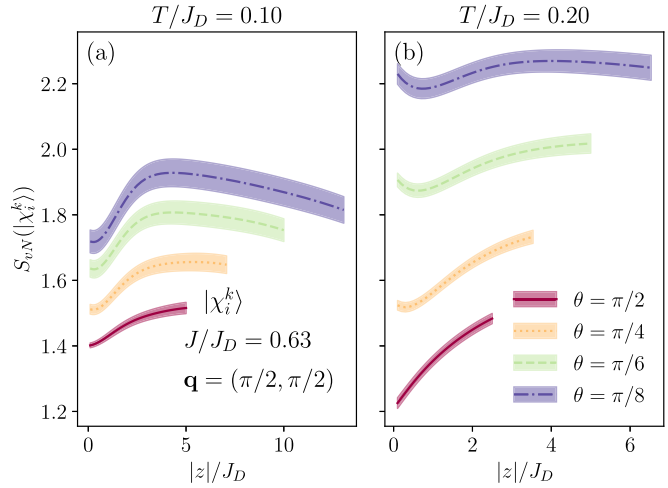



FIG. 9. Same as Fig. 8, but for the auxiliary state $|\chi_i^k\rangle$ Eq. (60).

The auxiliary state $|\phi_i^0\rangle = |\sigma_i\rangle$ is a classical product state such that the entropy in Fig. 8 starts from zero. Slower entanglement growth is observed for larger values of $\theta$ as expected. For $\theta = \pi/2$, we are performing fully imaginary-time evolution, which yields the slowest entanglement growth. Meanwhile, fluctuations of $S_{\mathrm{vN}}$ among the sampled states during METTS dynamics are rather small, as indicated by the shaded regions around the mean. The absolute values of $S_{\mathrm{vN}}$ are comparable for both $|\phi_i^k\rangle$ and $|\chi_i^k\rangle$ and grow with increasing temperature. We observe a significant reduction in entanglement entropy when comparing the values to the entanglement of the states $|v_i(t)\rangle$ [Eq. (18) as shown in Fig. 6]. While we observed maximal values of $S_{\mathrm{vN}} \approx 5.3$ for $T/J_D = 0.2$ for $|v_i(t)\rangle$ in Fig. 6, we only find maximal values of $S_{\mathrm{vN}} \approx 2.3$ for $\theta = \pi/8$ in Figs. 8 and 9. Naturally, the chosen time horizon $\Omega$ is significantly shorter when evaluating the analytical correlator. However, this demonstrates that $\mathcal{A}(z)$ can be evaluated at significantly reduced cost at nonzero values of $\theta$. We want to point out that setting a value of $\theta$ determines the allowed values of $\Omega$ because of the constraint $\Omega_\tau \leqslant \beta/2$ we impose for the analytical correlator. Hence, the maximal complex times $|z|$ differ for different values of $\theta$. In our simulations, the maximal computed entanglement entropy exhibits a plateau owing to simulating at finite bond dimension.

### C. Stochastic analytic continuation

To retrieve the spectral function from $\mathcal{A}(z)$, we perform analytic continuation, for which various approaches have been proposed and tested in the context of quantum Monte Carlo simulations [75–78]. We refer to the recent review [78] for a discussion of the challenges inherent to the analytic continuation of noisy data, as applied in the context of Monte Carlo simulations. The maximum-entropy [75] and stochastic analytic continuation (SAC) [76–78] methods have become default solutions for this task. Although mostly used for performing continuation of imaginary time correlation functions, these approaches are often also applicable for the analytic correlator $\mathcal{A}(z)$. In this case, we start closer to the real axis and we may therefore expect improved performance of conventional imaginary-time-based numerical analytic continuation approaches. Most importantly, the imaginary-time Green's function is dominated by the low-energy spectrum of the system whereas the high-energy part of the spectrum contributes significantly to the real-time correlator. Hence, analytic continuations from complex, rather than just imaginary-time Green's functions may help to resolve the spectrum.

We now document our SAC approach based on correlation functions in the complex time plane. In the following, we choose the observables to be $A^\dagger = B \equiv \mathcal{O}$. The aim is to obtain the finite temperature spectral function,

$$S(\omega) \equiv \frac{2\pi}{\mathcal{Z}} \sum_{m,n} e^{-\beta E_n} |\langle n|\mathcal{O}|m\rangle|^2 \delta(\omega - (E_n - E_m)), \quad (64)$$

where $|m\rangle$ ($|n\rangle$) is the $m$th ($n$th) eigenvector of the Hamiltonian with energy $E_m$ ($E_n$), cf. Eq. (34).

The correlation function is related to the spectral function via the following Laplacian transformation:

$$\begin{aligned}\mathcal{A}(z) &= \frac{1}{2\pi}\int_{-\infty}^{\infty} d\omega e^{-z\omega} S(\omega) \\ &= \frac{1}{2\pi}\int_{0}^{\infty} d\omega S(\omega)(e^{-z\omega} + e^{-(\beta-z)\omega}) \\ &\equiv \int_0^\infty d\omega A(\omega) K(z,\omega),\end{aligned} \quad (65)$$

where $S(-\omega) = e^{-\beta\omega} S(\omega)$ and we defined $A(\omega) \equiv S(\omega)(1 + e^{-\beta\omega})/2$ and the integration kernel as

$$K(z,\omega) \equiv (e^{-z\omega} + e^{-(\beta-z)\omega})(1 + e^{-\beta\omega})^{-1}\pi^{-1}, \quad (66)$$

which is by definition also a complex function. We parametrize $A(\omega)$ as a sum of delta functions,

$$A(\omega) = \sum_{i=1}^{N} A_i \delta(\omega - \omega_i). \quad (67)$$

During the stochastic sampling process, the testing Green's function is

$$\mathcal{A}^S(z) = \int_0^\infty d\omega A(\omega) K(z,\omega). \quad (68)$$

We stochastically sample the spectrum based on the following probability distribution:

$$P(A) \propto e^{-\chi^2(A)/\alpha}, \quad (69)$$

where the parameter $\alpha$ serves as a fictitious temperature that controls the Boltzmann weight of a given configuration, and $\chi^2(A)$ is the $\chi^2$ that measures the deviation of the correlation function based on any given $A(\omega)$ during stochastic sampling from the physical one that is observed from METTS calculations. As will be introduced in detail later, positions and amplitudes of the delta functions in Eq. (67) are shifted stochastically in a Monte Carlo sampling, such that the detailed balance condition is to fulfill the Gaussian probability $P(A)$.

In the current case, fluctuations from both real and imaginary parts of the correlation function are included in the definition of $\chi^2$,

$$\begin{aligned}\chi^2 \equiv \sum_{k=0}^{\Lambda/\delta_z}\sum_{k'=0}^{\Lambda/\delta_z} \big( &C^R_{kk'}{}^{-1}\mathrm{Re}(\mathcal{A}^S(z_k) - \overline{\mathcal{A}}(z_{k'}))^2 \\ &+ C^I_{kk'}{}^{-1}\mathrm{Im}(\mathcal{A}^S(z_k) - \overline{\mathcal{A}}(z_{k'}))^2\big),\end{aligned} \quad (70)$$

where $\overline{\mathcal{A}}(z_k)$ denotes the mean value of the analytic correlator at the $k$th time step $z_k = k\delta_z$. Note that generally we measure correlation function from $z_k = 0$ to $\Omega_z$. As expected, the SAC result depends weakly on the time cutoff $\Lambda$. So all data shown in the main text are based on the choice of $\Lambda \equiv \Omega_z$ such that the *analytic* correlation function from METTS simulation are entirely used. On the other hand, we show the cutoff dependence of SAC performance generally in Appendix G. The covariance matrices corresponding to the real and imaginary

parts of the correlator are defined, respectively,

$$C^R_{kk'} \equiv \frac{1}{R(R-1)} \sum_{i=1}^{R} \mathrm{Re}(\mathcal{A}^i(z_k) - \overline{\mathcal{A}}(z_k)) \times \mathrm{Re}(\mathcal{A}^i(z_{k'}) - \overline{\mathcal{A}}(z_{k'})),$$
$$C^I_{kk'} \equiv \frac{1}{R(R-1)} \sum_{i=1}^{R} \mathrm{Im}(\mathcal{A}^i(z_k) - \overline{\mathcal{A}}(z_k)) \times \mathrm{Im}(\mathcal{A}^i(z_{k'}) - \overline{\mathcal{A}}(z_{k'})), \quad (71)$$

where $\mathcal{A}^i(z_k)$ is the correlation function measured from the $i$th METTS state.

So far, the major difference between the current setup and the standard analytic continuation approach based on imaginary time correlation functions is the complexity of time $z$, correlation function $G(z)$, and the integration kernel $K(z, \omega)$.

As discussed extensively in imaginary-time-based SAC methods [77,79–82], large fluctuations are present at large $\alpha$, whereas the limit that $\chi^2$ approaches its minimal value in the infinitely small $\alpha$ limit leads to overfitted spurious peaks in the spectrum. Hence, the determination of the optimal fictitious sampling temperature $\alpha$ is a crucial issue. It relies on the dependence of the average $\chi^2$ on temperature $\alpha$, which is case dependent. As argued in Ref. [76], one suitable choice of $\alpha$ is the point where the *entropy* starts to drop from its maximum value via gradually decreasing $\alpha$. In practice, we perform an annealing process sequentially from $\alpha = 1$ to low temperature and pick $\alpha = \alpha_c$ as the one where the corresponding $\chi^2$ satisfies [78],

$$\chi^2 = \chi^2_{\min} + \sqrt{2S} \quad (72)$$

and we collect the averaged spectrum at the optimal $\alpha$. Instead of sampling at certain $\alpha_c$, an alternative approach is to average the sampled spectrum from temperature $\alpha = 1$ to a very low $\alpha$. We also tested this method via averaging over $\ln(1/\alpha) = 0, 0.1, 0.2, \ldots 6.0$ in the annealing process. Note that this is a weighted average and the weight is proportional to the slope of the $\chi^2$–$\alpha$ curve. Here, the former approach is a simple generalization of the one used in Ref. [78] to the complex plane, whereas the latter method, which was also frequently used in imaginary time cases, follows Ref. [77]. Details of the parameter dependence of the resulting spectral functions are presented in Appendix G.

We show the results of analytic continuation at $T/J_D = 0.1$ and 0.2 for several complex angles in Figs. 10 and 11. First, the spectrum obtained via the sampling at $\alpha_c$ does not differ from the one via weighted averaging the data from high to low fictitious temperature $\alpha$. Clearly, the position of the lowest triplon mode at $T/J_D = 0.1$ is consistent with both perturbation theory discussed in the companion paper [56] and the one from the *Hermitian* correlation function (at $\theta \to 0$ limit) as shown in Fig. 12 in the Appendix. Meanwhile, the second triplon peak at a higher frequency, which is not clearly visible for the case of $\theta = \pi/2$, can be resolved better from complex angle calculations. On the other hand, we did not observe a significant $\theta$ dependence for the thermal broadened spectrum at $T/J_D = 0.2$.

The optimal angle for calculating the analytic correlation function is a question of balancing the increased computational cost at a smaller complex angle and the higher uncertainty in analytical continuation at a larger one. Certainly, among the numerical cost-accessible regions in the complex time plane, one may push the calculation to the smallest possible complex angle to acquire the most accurate spectral function.

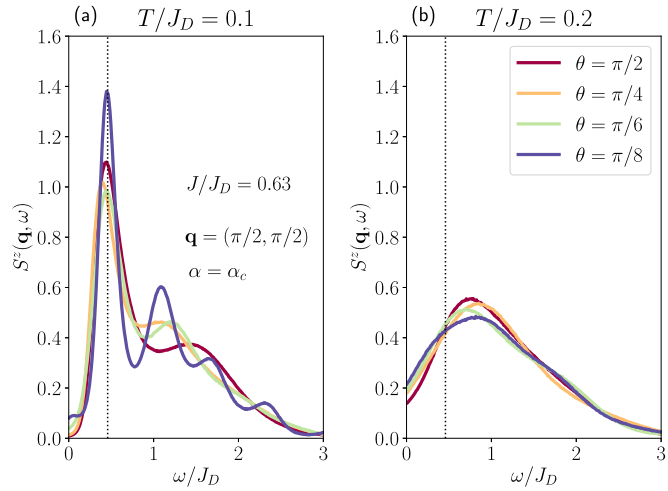



FIG. 10. Dynamical structure factors $S(\boldsymbol{q}, \omega)$ from stochastic analytic continuation based on analytic correlation functions $S(\boldsymbol{q}, z)$ at several complex angles. Here, the spectrum is obtained from sampling at $\alpha = \alpha_c$. Data are shown for the $16 \times 4$ lattice with $J/J_D = 0.63$ and $\boldsymbol{q} = (\pi/2, \pi/2)$. We compare between temperatures $T/J_D = 0.1$ (a) and $T/J_D = 0.2$ (b).

## V. DISCUSSION AND PERSPECTIVES

We introduced a method to compute dynamical spectral functions at nonzero temperatures. Compared to previous algorithms using MPS techniques [39–44], our method does not rely on purification but employs METTS states. The entanglement of the MPS states used in current computations can be reduced, enabling simulations of larger cylinder geometries. By performing a series of analyses, we propose

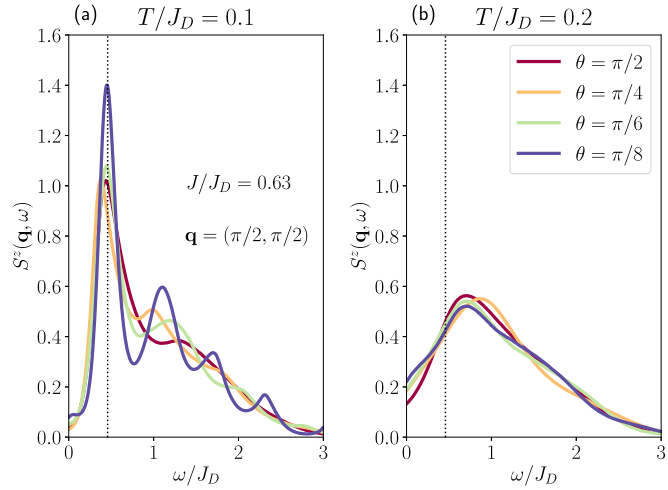



FIG. 11. Same as Fig. 10, where the spectrum is obtained via weighted averaging the collected histogram from $\ln\alpha = 0$ to $\ln\alpha = -6$.

that this method is capable of addressing questions in two-dimensional quantum magnets, exemplified by our study of the anomalous thermal broadening of $SrCu_2(BO_3)_2$ and the Shastry-Sutherland model [56].

The real-time evolution of METTS states is the computational bottleneck caused by the generically unbounded growth of entanglement. The scaling of the method is determined by the maximal MPS and matrix-product operator bond dimensions needed for accurate simulation. The scaling of the methods we propose here is the same as DMRG, since we are using the TDVP time-evolution method. To alleviate the difficulties arising from large bond dimensions, we suggest that complex-time correlators can be used to lower the computational cost. The key idea is that a contribution from imaginary-time evolution with a negative exponent will ultimately evolve the METTS state to the ground state, for which entanglement bounds are known. While complex-time evolution had been proposed for QMC [51] or MPS methods at $T = 0$ applied to impurity models [52,53], we here propose algorithms that employ this approach at nonzero temperatures using METTS with MPS.

We considered two different ways of generalizing time-dependent correlation functions to complex time, which we denote by the *analytic* and *Hermitian* correlation functions. The analytic one is a natural generalization of the spectrum in the Matsubara formalism to the complex plane, such that conventional numerical analytic continuation approaches can be easily generalized correspondingly. Most importantly, real-time contribution to the time-displaced correlator improves the quality of analytic continuation. Reference [52] also provided an alternative method for performing the continuation from the complex plane, which could presumably also be applied to the present case.

On the other hand, the definition of the *Hermitian* correlator has the advantage of easy implementation and the imaginary-time evolution dissipates the entanglement entropy dramatically. Meanwhile, the main structure of the real-frequency spectrum is well captured even in the presence of a systematic deviation because of imaginary-time contributions. Only recently, this version of a complex-time correlator has been studied [53] in the context of impurity models with MPS. Moreover, Ref. [53] provides a method of extrapolating correlation functions from the complex plane to the real axis, which demonstrably is capable of achieving high accuracy.

It is worth pointing out that the idea of introducing an imaginary-time component to reduce entanglement is similar in spirit to the dissipation-assisted operator evolution proposed in Ref. [45]. The imaginary-time component acts as a natural "dissipator". One advantage of the present approach is that existing implementations of time-evolution algorithms, such as TDVP, can be readily employed to compute complex-time evolution.

The SAC method based on the *analytic* correlation function offers yet further possibilities for future improvement: one promising suggestion is to perform continuation via combined information of correlators at several angles along the complex plane. Apart from the stochastic approach, an interesting direction is to combine the Nevanlinna analytic continuation [83] approach with the correlation functions obtained from certain METTS states. On the other hand, a common technique for computing dynamical spectral functions at zero temperature by using real-time evolution with MPS, is to perform linear prediction in order to extend the time-series of correlation functions [39,84–86]. While it is reported that this works remarkably well for simple spectra with few poles, we have not been able to successfully apply this to the correlation functions computed at nonzero temperatures in this work. For generic METTS states, we mostly find strong disagreement between the actual time evolution and the linear prediction. This is likely because of the fact that the correlators $\mathcal{C}_i(t)$ from METTS in general have a more complex structure than a superposition of a few sinusoidal waves. Thus, all the data we present are taken from actual-time evolution. Recently, however, a more advanced method for performing linear prediction in the context of spectral functions with increased accuracy has been proposed [86]. It would be interesting to find out whether this method would be beneficial in the present context to extend the METTS time series.

In summary, we demonstrated that the combination of METTS with either real or complex-time evolution can be applied to study spectral functions of two-dimensional quantum many-body systems using MPS. While the most accurate approach using real-time correlation functions is feasible on certain problem sizes, the complex-time correlation functions can be evaluated more efficiently. The reduction of computation cost can be tuned using the complex angle $\theta$, from highly accurate but less efficient at $\theta$ close to zero to highly efficient but less accurate at larger values of $\theta$. We, therefore, propose this method to serve as a bridge between the physics of quantum lattice models and spectroscopy experiments performed on strongly correlated materials.

## ACKNOWLEDGMENTS

Z.W. thanks Anders Sandvik and Hui Shao for enlightening discussions on the stochastic analytic continuation method. A.W. is grateful to Siddharth Parameswaran, Roderich Moessner, Miles Stoudenmire, and Olivier Parcollet for insightful discussions. Exact diagonalization calculations have been performed using the XDIAG package [87]. A.W. acknowledges support by the DFG through the Emmy Noether program (Grant No. 509755282). Z.W. was supported by the FP7/ERC Consolidator Grant QSIMCORR, No. 771891 and by the Deutsche Forschungsgemeinschaft (DFG, German Research Foundation) under Germany's Excellence Strategy – EXC-2111 – 390814868.

## APPENDIX A: HERMITIAN COMPLEX-TIME CORRELATION FUNCTIONS

Here, we discuss the second possible generalization of correlation functions to complex time, the Hermitian correlation function as defined in Eq. (44), which expanded in the METTS basis yields

$$\mathcal{H}_{AB}(z) = \langle e^{iHz^\star} A e^{-iHz} B\rangle \tag{A1}$$

$$= \frac{1}{\mathcal{Z}} \sum_i p_i \langle\psi_i| e^{iHz^\star} A e^{-iHz} B|\psi_i\rangle \tag{A2}$$

$$= \frac{1}{\mathcal{Z}} \sum_i p_i \mathcal{H}^i_{AB}(z), \tag{A3}$$

where we define the sample Hermitian correlation function as

$$\mathcal{H}^i_{AB}(z) \equiv \langle\psi_i|e^{iHz^\star}Ae^{-iHz}B|\psi_i\rangle. \tag{A4}$$

To evaluate this correlation function, we can proceed analogously to the conventional time-dependent correlation function algorithm in Algorithm 1, and define the states

$$|v_i(z)\rangle = e^{-iHz}B|\psi_i\rangle = e^{-H\tau}e^{-iHt}B|\psi_i\rangle, \tag{A5}$$

$$|w_i(z)\rangle = e^{-iHz}|\psi_i\rangle = e^{-H\tau}e^{-iHt}|\psi_i\rangle. \tag{A6}$$

Using these states, we evaluate the sample Hermitian correlation functions as

$$\mathcal{H}^i_{AB}(z) = \langle w_i(z)|A|v_i(z)\rangle, \tag{A7}$$

using Algorithm 1 adjusted for the complex-time evolution along the contour $z = |z|e^{-i\theta}$ shown in Fig. 7. A key difference to the dynamical METTS Algorithm 1 is the fact that the time-evolution operators $e^{-iHz}$ and $e^{iHz^\star}$ are not norm preserving. However, we could reenforce a normalization by setting

$$n_v^2 \equiv \langle v_i(z)|v_i(z)\rangle = \langle\psi_i|B^\dagger e^{-2\tau H}B|\psi_i\rangle, \tag{A8}$$

$$n_w^2 \equiv \langle w_i(z)|w_i(z)\rangle = \langle\psi_i|e^{-2\tau H}|\psi_i\rangle, \tag{A9}$$

$$c_B^2 \equiv \langle\psi_i|B^\dagger B|\psi_i\rangle \tag{A10}$$

and introducing the modified states,

$$|\tilde{v}_i(z)\rangle = c_B\,|\tilde{v}_i(z)\rangle/n_v = c_B\,e^{-iHt}e^{-H\tau}B|\psi_i\rangle/n_v, \tag{A11}$$

$$|\tilde{w}_i(z)\rangle = |\tilde{w}_i(z)\rangle/n_w = e^{-iHt}e^{-H\tau}|\psi_i\rangle/n_w. \tag{A12}$$

Finally, we consider the modified sample Hermitian correlation functions,

$$\tilde{\mathcal{H}}^i_{AB}(z) = \langle\tilde{w}_i(z)|A|\tilde{v}_i(z)\rangle, \tag{A13}$$

giving rise to a modified Hermitian correlation function

$$\tilde{\mathcal{H}}_{AB}(z) = \frac{1}{\mathcal{Z}}\sum_i p_i\tilde{\mathcal{H}}^i_{AB}(z). \tag{A14}$$

Our strategy is to directly view $\tilde{\mathcal{H}}_{AB}(z)$ as an approximation of $\mathcal{C}_{AB}(t)$,

$$\mathcal{C}_{AB}(t) \approx \tilde{\mathcal{H}}_{AB}(t - it\tan\theta). \tag{A15}$$

We find that $\tilde{\mathcal{H}}_{AB}(z)$ is a significantly better approximation to $\mathcal{C}_{AB}(t)$ than the bare Hermitian correlator $\mathcal{H}_{AB}(z)$, which motivates the modified definition.

The negative signs in the real exponentials $e^{-H\tau}$ lead to stability of computing $e^{-H\tau}|\psi\rangle$, where $|\psi\rangle$ denotes an arbitrary wave function. Moreover, evaluating imaginary-time evolutions $e^{-H\tau}|\psi\rangle$ with a negative prefactor is well suited for MPS methods. Whenever the overlap with the groundstate $|\psi_0\rangle$ of $H$ is nonzero, i.e., $\langle\psi_0|\psi\rangle \neq 0$, we have

$$\lim_{\tau\to\infty} e^{-H\tau}|\psi\rangle \simeq |\psi_0\rangle. \tag{A16}$$

Since ground states of local Hamiltonians are subject to bounds on their entanglement, we also expect states of the form $e^{-H\tau}|\psi\rangle$ to have manageable entanglement, whenever $|\psi\rangle$ is weakly entangled.

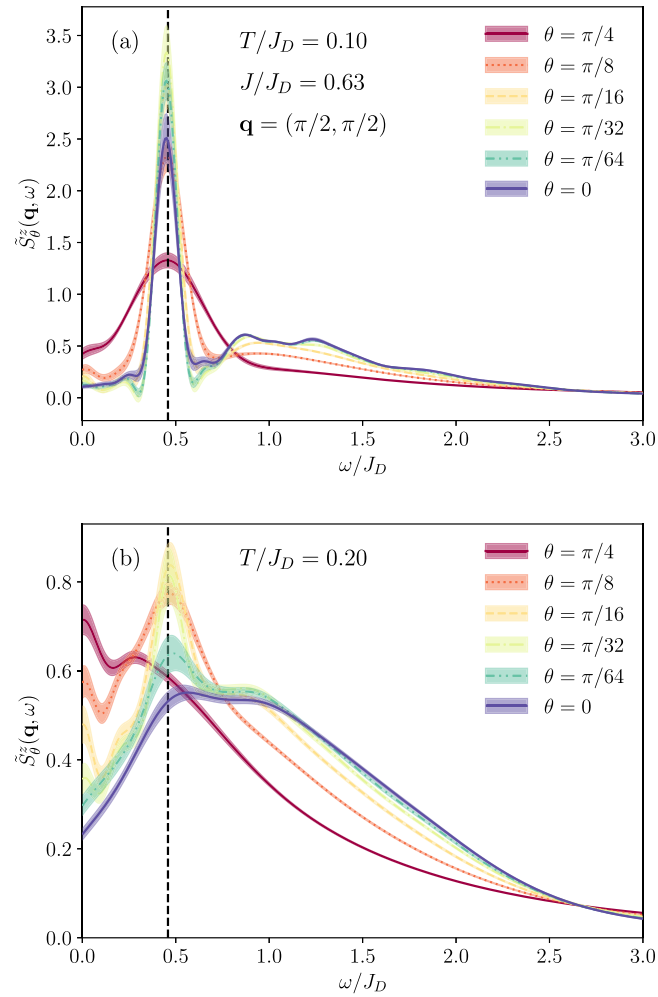



FIG. 12. Hermitian dynamical structure factors $\tilde{S}^z_\theta(\boldsymbol{q}, \omega)$ from complex-time correlation functions $\tilde{S}^z_\theta(\boldsymbol{q}, t)$ at different complex angles $\theta$. Data are shown for the $16 \times 4$ lattice with $J/J_D = 0.63$ and $\boldsymbol{q} = (\pi/2, \pi/2)$. We compare between temperatures $T/J_D = 0.1$ (a) and $T/J_D = 0.2$ (b). We observe that several key features of the exact spectral function $S(\boldsymbol{q}, \omega)$ ($\theta = 0$) are already captured well by sizable values of $\theta$. Larger values of $\theta$ significantly reduce the computational cost. Time evolution has been performed up to time $\Omega/J_D = 50$ for $R = 100$ samples.

We show Hermitian spectral functions $S^z_\theta(\boldsymbol{q}, \omega)$ for the $16 \times 4$ Shastry-Sutherland lattice at $J/J_D = 0.63$ and temperatures $T/J_D = 0.1, 0.2$ in Fig. 12. Remarkably, for $T/J_D = 0.1$, the position of the dominant peak at $\omega/J_D \approx 0.458$ is always obtained consistently even for sizable values of the complex angle $\theta$. Meanwhile, the height and width of the dominant peak are well captured as long as $\theta \leqslant \pi/16$. Moreover, even features like secondary peaks at higher temperatures are captured correctly for not too large values of the complex angle $\theta$. Similarly, the overall shape of the exact spectral function with $\theta = 0$ at $T/J_D = 0.2$ in Fig. 12(b) is generally well captured at larger values of $\theta$. However, the peak around the triplon gap for $\omega/J_D \approx 0.458$ is overestimated at finite angles of $\theta$.

Our main motivation for employing the Hermitian correlation function is to limit the entanglement when time-evolving

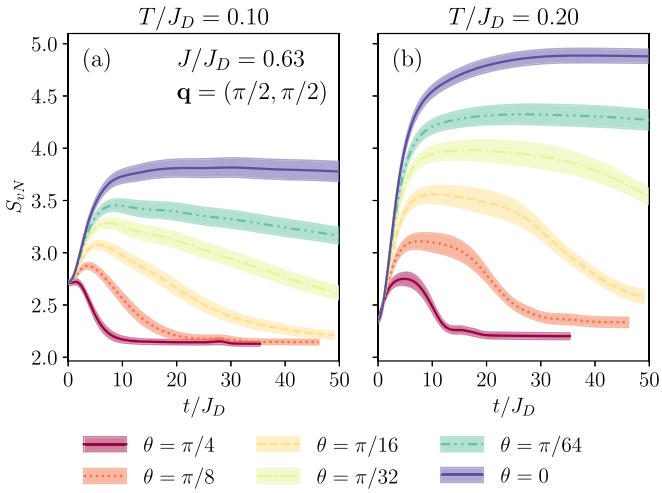



FIG. 13. Average bipartite von Neumann entanglement entropy $S_{\text{vN}}$ of the states $|\tilde{v}_i(z)\rangle$ as in Eq. (A11) for computing the Hermitian correlator Eq. (44). Data on the $16 \times 6$ Shastry-Sutherland lattice for different values of the complex angle $\theta$ at $J/J_D = 0.63$ and $\boldsymbol{q} = (\pi/2, \pi/2)$. We compare results for temperatures $T/J_D = 0.1$ (a) and $T/J_D = 0.2$ (b). For larger values of $\theta$, we observe convergence of $S_{\text{vN}}$ towards the ground-state entanglement entropy.

an MPS state. Thus, we show the average growth of the bipartite von Neumann entropy $S_{\text{vN}}$ of the states $|\tilde{v}_i(z)\rangle$ for different values of $\theta$ on a $16 \times 6$ cylinder in Fig. 13. We chose momenta $\boldsymbol{q} = (\pi/2, \pi/2)$, $J/J_D = 0.63$ and temperatures $T/J_D = 0.1, 0.2$. As expected, for $\theta = 0$ the entanglement is monotonically growing as a function of time. While the initial entanglement of the METTS state at $T/J_D = 0.1$ in (a) is larger than at $T/J_D = 0.2$ in (b), the entanglement grows more quickly when going to higher temperatures. As soon as $\theta > 0$ we observe an initial growth of the entanglement, followed by a decay caused by the imaginary-time evolution component when applying $e^{-\tau H}$. We see at nonzero values of $\theta$ that entanglement is quickly suppressed after attaining an intermediate maximum which grows when decreasing $\theta$. We thus conclude that a nonzero complex angle $\theta$ solves the issue of unbounded entanglement growth at the cost of introducing a controlled error when evaluating the spectral functions.

## APPENDIX B: GEOMETRY OF THE SIMULATION CYLINDER

In the main text, we use simulations on several $L \times W$ cylinder systems, where we apply periodic boundary conditions in the short direction $W$ and open boundary conditions in the long direction $L$. We use a square geometry for the Shastry-Sutherland lattice, where we define the unit cell, consisting of four basis sites, by the unit vectors,

$$\boldsymbol{a}_1 = (2, 0), \quad \boldsymbol{a}_2 = (0, 2), \tag{B1}$$

and the basis coordinates are given by

$$\boldsymbol{b}_1 = (0, 0), \quad \boldsymbol{b}_2 = (1, 0), \tag{B2}$$

$$\boldsymbol{b}_3 = (0, 1), \quad \boldsymbol{b}_4 = (1, 1). \tag{B3}$$

As such the momenta $\boldsymbol{k} = (k_x, k_y)$ in the first Brillouin zone satisfy $k_x, k_y \in [-\pi/2, \pi/2]$ and in the extended Brillouin zone $k_x, k_y \in [-\pi, \pi]$. We show the geometry of a $16 \times 4$ cylinder in Fig. 14(a) and the Brillouin zone in Fig. 14(b), where we marked the momenta investigated in the main text with red circles.

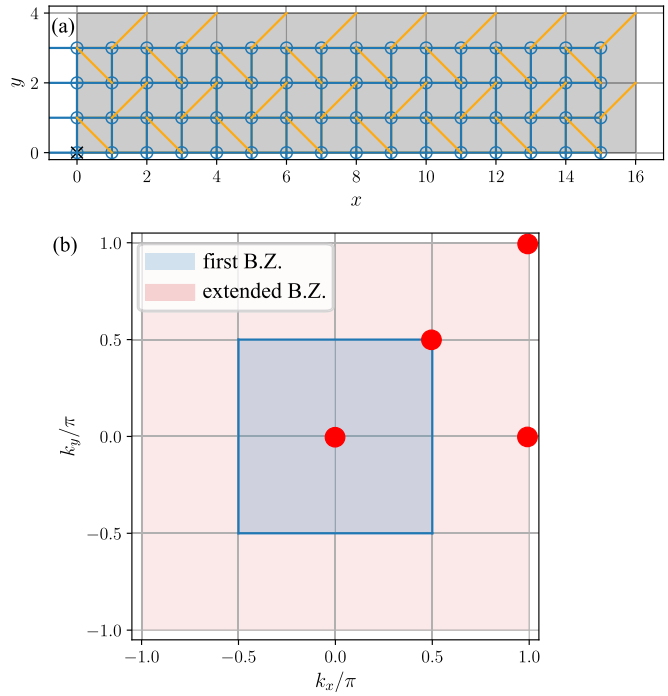



FIG. 14. (a) Geometry of the $16 \times 4$ Shastry-Sutherland lattice used in the main text. (b) First and extended Brillouin zone of the lattice, with momenta $\boldsymbol{k} = (0, 0), (\pi/2, \pi/2), (\pi, 0), (\pi, \pi)$ marked with red circles.

## APPENDIX C: PROJECTION ERROR OF TDVP

One potential error of the TDVP method exists at the step of projecting the time-dependent Schrödinger equation onto the relevant MPS subspace [68]. This projection error is especially severe when time evolving an MPS with very low bond dimension. It turns out to be a serious issue for the Shastry-Sutherland model when the temperature is much lower than the first triplon gap $\Delta$. In this low-energy case, the MPS during the time-evolution step does not differ significantly from the ground state, which is known to be a product state of spin singlets living on the diagonal bonds. The projection error leads to a biased estimation of the spin gap, even with the two-site TDVP approach. On the other hand, time-evolving block decimation (TEBD) suffers only from the Trotter error and the MPS truncation error.

As a test, we show a comparison between TDVP and TEBD methods in Fig. 15. At low temperatures, one expects the imaginary time correlation function to decay with an exponential factor based on the estimated spin gap ($\Delta \approx 0.458 J_D$) from the perturbation theory. However, as can be seen from the plot, $G(\tau)$ obtained from the two-site TDVP method deviates from this expectation with a much steeper slope, for $T/\Delta = 0$ and 0.1. On the other hand, the long-time correlation from TEBD resolves the expected spin gap. Meanwhile, for temperatures comparable with the spin gap, enough entangle-

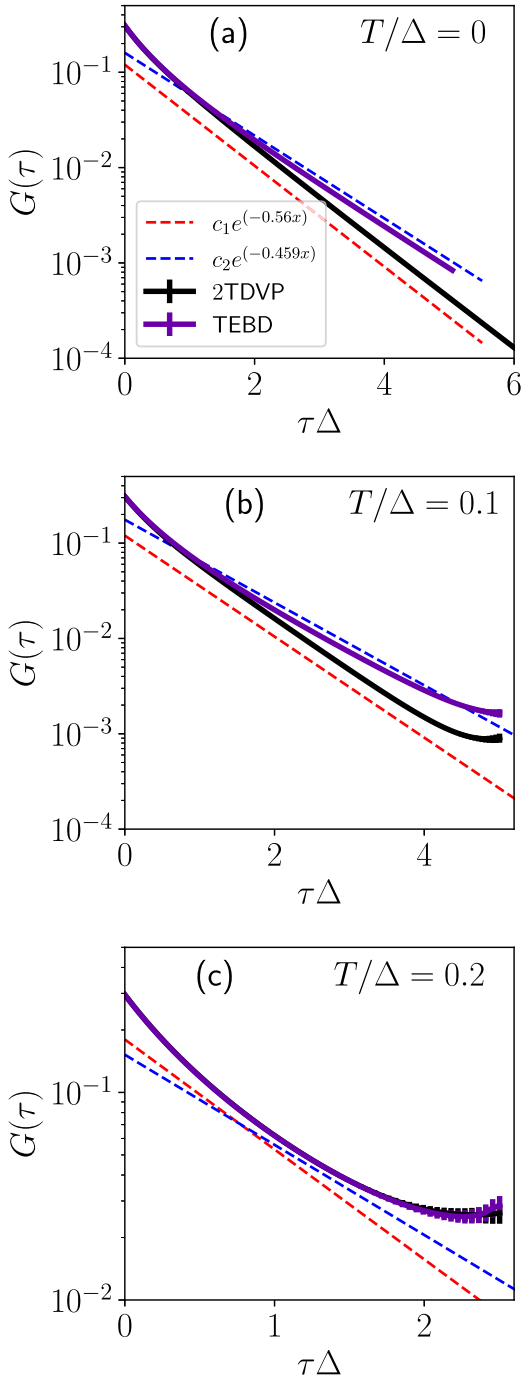



FIG. 15. Imaginary time correlation function using TEBD and the two-site TDVP approach, for $T/\Delta = 0$ (a), 0.1 (b), and 0.2 (c) on the $16 \times 4$ cylinder. Two dashed lines, including $c_2 e^{-\Delta\tau}(\Delta \approx 0.458)$ and $c_1 e^{-0.56\tau}$ are guides to the eye. The time-evolution approach for measuring correlation functions at $T = 0$ is based on the ground state via DMRG calculation, where the ones at $T/J_D = 0.1$ and 0.2 are from averaging the METTS configurations.

ment is built up within the time-evolved MPS and we do not observe a severe projection error in TDVP. This can be seen from the consistent data between the two methods at $T/\Delta = 0.2$. For the three temperatures shown here, we choose the time step in TEBD as $d\tau = 0.1$ such that the Trotter error is sufficiently small.

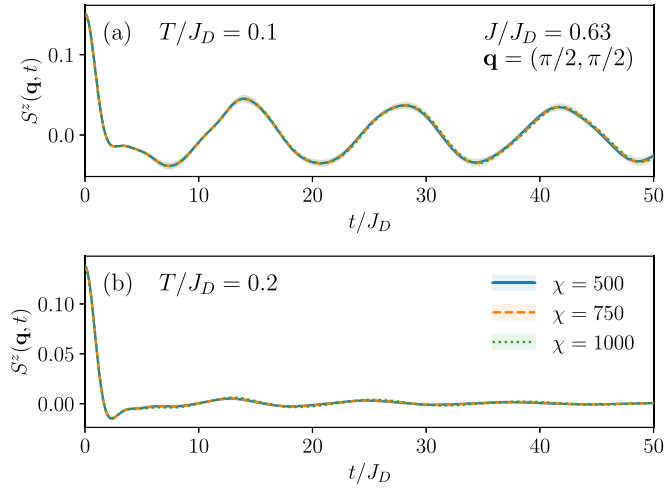



FIG. 16. Convergence of the time-dependent correlation function $S^z(\boldsymbol{q}, t)$ for $J/J_D = 0.63$ and $\boldsymbol{q} = (\pi/2, \pi/2)$ on the $16 \times 4$ cylinder. We show results for two temperatures, (a) $T/J_D = 0.1$, and (b) $T/J_D = 0.2$, and compare bond dimensions $\chi = 500, 750, 1000$. We observe convergence for all times within the statistical error bars.

## APPENDIX D: CONVERGENCE IN MPS BOND DIMENSION

As we are using the METTS algorithm together with matrix-product state time evolution, we analyze the convergence of the dynamical correlations in the MPS bond dimension. In Fig. 16, we show results for the real-time dynamical correlation function $S^z(\boldsymbol{q}, t)$ on a $16 \times 4$ cylinder. The model parameters have been chosen as $J/J_D = 0.63$ with temperatures (a) $T/J_D = 0.1$, and (b) $T/J_D = 0.2$, and wave vector $\boldsymbol{q} = (\pi/2, \pi/2)$. We compare results from TDVP simulations at bond dimensions $\chi = 500, 750, 1000$, which exhibit convergence within the statistical error bars from METTS sampling. As such, we can conclude that a moderate bond dimension of $\chi = 500$ is sufficient to accurately resolve the spectra we investigate on the $16 \times 4$ cylinder.

## APPENDIX E: COMPARISON OF WINDOWING FUNCTIONS

In this Appendix we compare the results of computing the spectral functions using different windowing functions to perform the Fourier transform. In the main text in Fig. 4, we used the Hann window of the form

$$w(x) = 0.5 + 0.5\cos(\pi x) \quad \text{for} \quad 0 \leqslant |x| \leqslant 1. \tag{E1}$$

One could ask to what extent the result depends on the windowing function. To answer this question, we compare two different windowing functions. First, we show results using the Parzen window of the form

$$w(x) = \begin{cases} 1 - 6|x|^2 + 6|x|^3 & \text{if} \quad 0 \leqslant |x| \leqslant 1/2 \\ 2(1 - |x|^3) & \text{if} \quad 1/2 \leqslant |x| \leqslant 1 \end{cases}, \tag{E2}$$

in Fig. 17. The Parzen windowing function has previously been used in the context of time-dependent DMRG at zero temperature [20].

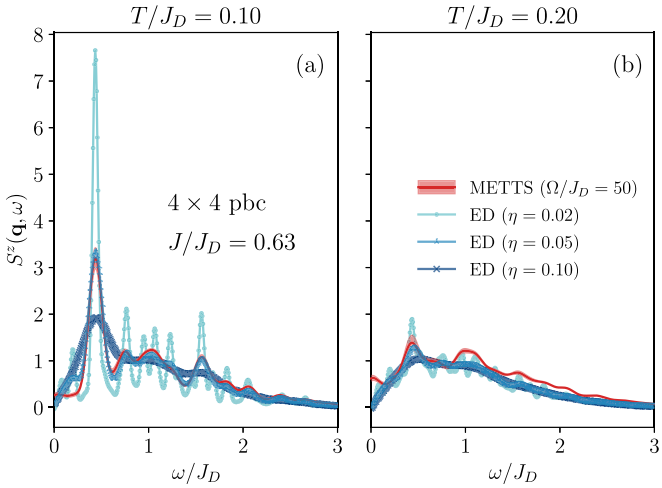



FIG. 17. Comparison of spectral functions obtained via ED and the real-time METTS algorithm as in Fig. 4, but using a Parzen windowing function Eq. (E2).

An equally valid choice of windowing function is a Gaussian window of the form

$$w(x) = \exp\left(-\frac{|x|^2}{2\sigma^2}\right) \quad \text{for} \quad 0 \leqslant |x| \leqslant 1, \qquad \text{(E3)}$$

where $\sigma$ controls the width of the Gaussian window. Results from applying the Gaussian windowing function with $\sigma = 1/2$ are shown in Fig. 18.

Overall, we see that because of the chosen maximal simulation time $\Omega/J_D = 50$, our results are not strongly affected by the choice of windowing function. The effects of the windowing function are expected to vanish for $\Omega \to \infty$.

## APPENDIX F: COMPARISON WITH TIME-EVOLUTION FROM EXACT DIAGONALIZATION

In the main text, we compare the spectral function obtained using the dynamical METTS algorithm with a spectral function obtained using the Lehmann representation with exact pole positions and weights in Fig. 4. A noticeable difference is a discrepancy close to $\omega = 0$, which is argued to stem from the finite-time horizon in the dynamical METTS simulations. Here, we demonstrate that this indeed is the case by comparing the time-dependent correlation functions $C_{AB}(t)$ obtained from dynamical METTS with exact diagonalization data on a $4 \times 4$ cluster. In Fig. 19(a), we compare both the time-dependent correlation function $C_{AB}(t)$ obtained from dynamical METTS and full exact diagonalization, where we find agreement within the error bars. We then obtain the spectral function $C_{AB}(\omega)$ from exact diagonalization by Fourier transforming the time-dependent correlation function in the same manner as the dynamical METTS samples are Fourier transformed. A comparison between the methods is shown in Fig. 19(b), where again agreement within error

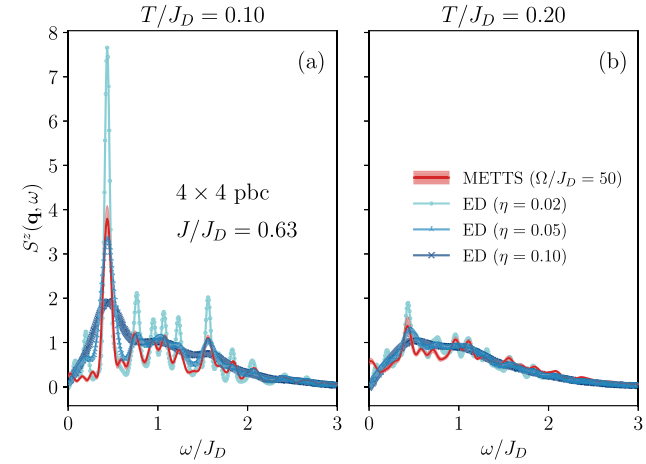



FIG. 18. Comparison of spectral functions obtained via ED and the real-time METTS algorithm as in Fig. 4, but using a Gaussian windowing function Eq. (E3) of width $\sigma = 1/2$.

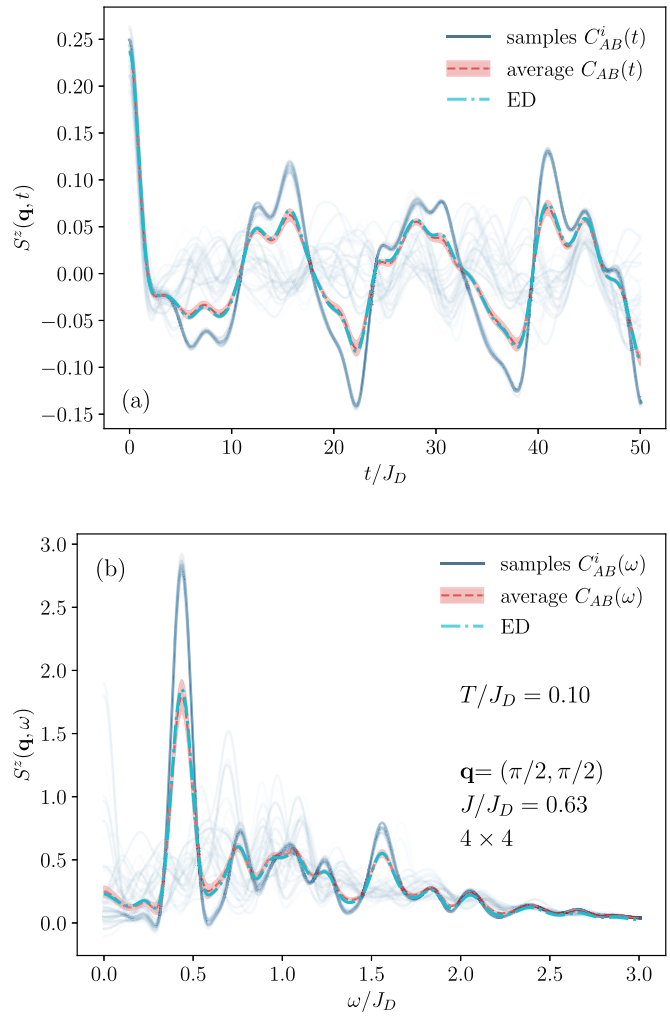



FIG. 19. (a) Comparison of the time-dependent correlation function $C_{AB}(t)$ obtained from dynamical METTS (red, dashed line) with full exact diagonalization (cyan, dashdotted line) from $R = 100$ METTS samples. We used $A^\dagger = B = S^z(\boldsymbol{q})$ with $\boldsymbol{q} = (\pi/2, \pi 2)$ on a $4 \times 4$ geometry with periodic boundary conditions at temperature $T/J_D = 0.10$ and $J/J_D = 0.63$. Blue solid lines show the sample correlations $C^i_{AB}(t)$. (b) Comparison of the spectral function $C_{AB}(\omega)$. We observe agreement within the error bars.

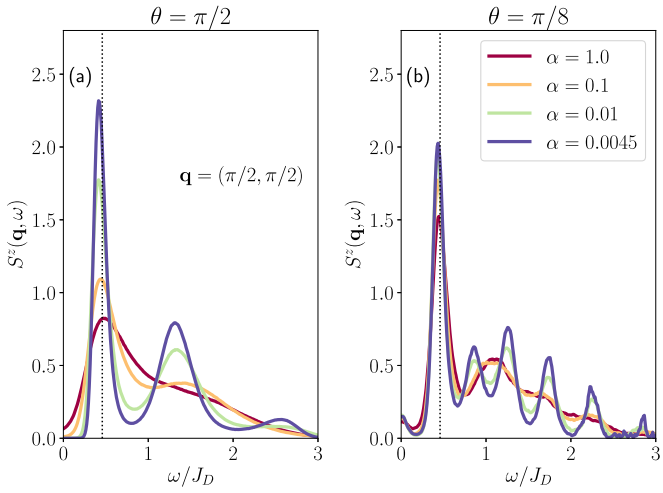



FIG. 20. $S(\boldsymbol{q}, \omega)$ from stochastic analytic continuation at $\alpha = 1.0, 0.1, 0.01$, and $0.0045$, based on $S(\boldsymbol{q}, z)$ at $\theta = \pi/2$ (a) and $\pi/8$ (b), for $T/J_D = 0.1$ on the $16 \times 4$ cylinder. The simulations at different $\alpha$ are performed via independent annealing processes from high temperatures.

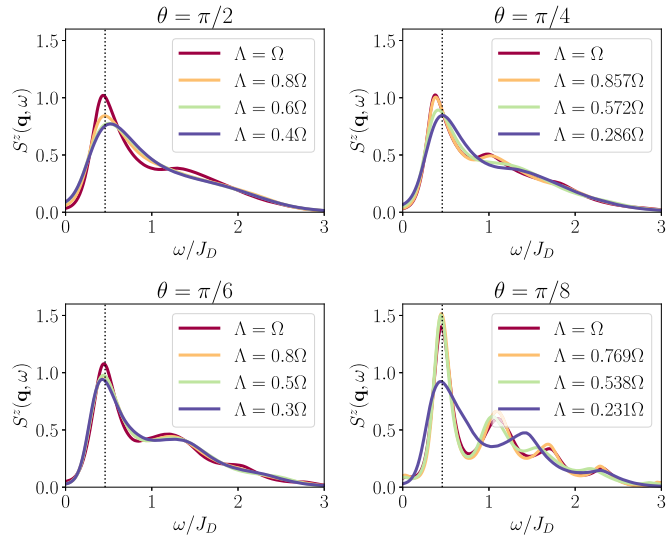



FIG. 21. Cutoff dependence of the dynamical correlator of $S^z$ for $\theta = \pi/2, \pi/4, \pi/6$ and $\pi/8$. $\Lambda$ denotes the maximum value of time that is used in SAC.

bars is observed. We can, thus, conclude that the differences of the dynamical METTS algorithm with the Lehmann representation from exact diagonalization are rooted in the finite-simulation time horizon $\Omega$.

## APPENDIX G: FICTITIOUS TEMPERATURE DEPENDENCE OF STOCHASTIC ANALYTIC CONTINUATION

In the SAC sampling process, one normally expects a characteristic *thermal phase transition temperature* where the specific heat shows a jump. However, in the SAC process based on our METTS data on the $16 \times 4$ Shastry-Sutherland lattice, $\chi^2$ decays toward $\chi^2_{\min}$ smoothly as a function of the fictitious temperature $\alpha$. Hence, we choose to use the weighted average of the spectrum over a wide range of $\alpha$. It is, nevertheless, important to check the $\alpha$ dependence of the spectrum, and especially to compare between the imaginary and complex time cases.

We choose the same set of METTS data that is used in Sec. IV C as showcased here. As depicted in Fig. 20, the spectral function obtained via the imaginary time $\theta = \pi/2$ correlator depends strongly on the choice of $\alpha$. Taking the spectrum in Fig. 12 as a reference, the weight and position of the second triplon peak are clearly biased for both $\alpha = 0.01$ and $0.0045$. On the other hand, the overall shape of the spectrum at $\theta = \pi/8$ is much more stable, although we observe an unphysical splitting of the second peak at small $\alpha$.

In Sec. IV C, no explicit time-domain cutoff was taken into consideration for the analytic continuation approach. Here, we show the spectral function at $T = 0.1$ as a function of cutoff in Fig. 21. Instead of choosing $z \in [0, \Omega_z]$ ($\Omega_z = \beta/(2\cos\theta)$), as introduced in the main text such that no data points are discarded for the SAC calculation, here we choose a truncation in the time axis. As shown in the plot, using the time domain of $z \in [0, \Lambda]$ ($\Lambda \leqslant \Omega_z$), the spectral function that we obtain from analytic continuation has a weak cutoff dependence at small $\theta$ and large $\Lambda$.


[1] J. Gubernatis, N. Kawashima, and P. Werner, *Quantum Monte Carlo Methods: Algorithms for Lattice Models* (Cambridge University Press, Cambridge, 2016).

[2] E. Y. Loh, J. E. Gubernatis, R. T. Scalettar, S. R. White, D. J. Scalapino, and R. L. Sugar, Sign problem in the numerical simulation of many-electron systems, Phys. Rev. B **41**, 9301 (1990).

[3] R. Orús, Tensor networks for complex quantum systems, Nat. Rev. Phys. **1**, 538 (2019).

[4] M. C. Bañuls, Tensor network algorithms: A route map, Annu. Rev. Condens **14**, 173 (2023).

[5] S. R. White, Density matrix formulation for quantum renormalization groups, Phys. Rev. Lett. **69**, 2863 (1992).

[6] S. R. White, Density-matrix algorithms for quantum renormalization groups, Phys. Rev. B **48**, 10345 (1993).

[7] U. Schollwöck, The density-matrix renormalization group, Rev. Mod. Phys. **77**, 259 (2005).

[8] U. Schollwöck, The density-matrix renormalization group in the age of matrix product states, Ann. Phys. **326**, 96 (2011).

[9] X. Wang and T. Xiang, Transfer-matrix density-matrix renormalization-group theory for thermodynamics of one-dimensional quantum systems, Phys. Rev. B **56**, 5061 (1997).

[10] B. Ammon, M. Troyer, T. M. Rice, and N. Shibata, Thermodynamics of the $t$-$J$ ladder: A stable finite-temperature density matrix renormalization group calculation, Phys. Rev. Lett. **82**, 3855 (1999).

[11] A. E. Feiguin and S. R. White, Finite-temperature density matrix renormalization using an enlarged Hilbert space, Phys. Rev. B **72**, 220401(R) (2005).

[12] S. R. White, Minimally entangled typical quantum states at finite temperature, Phys. Rev. Lett. **102**, 190601 (2009).

[13] E. M. Stoudenmire and S. R. White, Minimally entangled typical thermal state algorithms, New J. Phys. **12**, 055026 (2010).

[14] A. Wietek, Y.-Y. He, S. R. White, A. Georges, and E. M. Stoudenmire, Stripes, antiferromagnetism, and the pseudogap in the doped Hubbard model at finite temperature, Phys. Rev. X **11**, 031007 (2021).

[15] A. Wietek, R. Rossi, F. Šimkovic, M. Klett, P. Hansmann, M. Ferrero, E. M. Stoudenmire, T. Schäfer, and A. Georges, Mott insulating states with competing orders in the triangular lattice Hubbard model, Phys. Rev. X **11**, 041013 (2021).

[16] C. Feng, A. Wietek, E. M. Stoudenmire, and R. R. P. Singh, Order, disorder, and monopole confinement in the spin-$\frac{1}{2}$ XXZ model on a pyrochlore tube, Phys. Rev. B **106**, 075135 (2022).

[17] C. Feng, E. M. Stoudenmire, and A. Wietek, Bose-Einstein condensation in honeycomb dimer magnets and $Yb_2Si_2O_7$, Phys. Rev. B **107**, 205150 (2023).

[18] A. Nocera and G. Alvarez, Symmetry-conserving purification of quantum states within the density matrix renormalization group, Phys. Rev. B **93**, 045137 (2016).

[19] K. A. Hallberg, Density-matrix algorithm for the calculation of dynamical properties of low-dimensional systems, Phys. Rev. B **52**, R9827 (1995).

[20] T. D. Kühner and S. R. White, Dynamical correlation functions using the density matrix renormalization group, Phys. Rev. B **60**, 335 (1999).

[21] S. R. White and A. E. Feiguin, Real-time evolution using the density matrix renormalization group, Phys. Rev. Lett. **93**, 076401 (2004).

[22] P. E. Dargel, A. Honecker, R. Peters, R. M. Noack, and T. Pruschke, Adaptive Lanczos-vector method for dynamic properties within the density matrix renormalization group, Phys. Rev. B **83**, 161104(R) (2011).

[23] A. Holzner, A. Weichselbaum, I. P. McCulloch, U. Schollwöck, and J. von Delft, Chebyshev matrix product state approach for spectral functions, Phys. Rev. B **83**, 195115 (2011).

[24] P. E. Dargel, A. Wöllert, A. Honecker, I. P. McCulloch, U. Schollwöck, and T. Pruschke, Lanczos algorithm with matrix product states for dynamical correlation functions, Phys. Rev. B **85**, 205119 (2012).

[25] A. Nocera and G. Alvarez, Spectral functions with the density matrix renormalization group: Krylov-space approach for correction vectors, Phys. Rev. E **94**, 053308 (2016).

[26] M. Gohlke, R. Verresen, R. Moessner, and F. Pollmann, Dynamics of the Kitaev-Heisenberg model, Phys. Rev. Lett. **119**, 157203 (2017).

[27] R. Verresen, R. Moessner, and F. Pollmann, Avoided quasiparticle decay from strong quantum interactions, Nat. Phys. **15**, 750 (2019).

[28] M. Drescher, L. Vanderstraeten, R. Moessner, and F. Pollmann, Dynamical signatures of symmetry-broken and liquid phases in an $S = \frac{1}{2}$ Heisenberg antiferromagnet on the triangular lattice, Phys. Rev. B **108**, L220401 (2023).

[29] G. Vidal, Efficient simulation of one-dimensional quantum many-body systems, Phys. Rev. Lett. **93**, 040502 (2004).

[30] A. J. Daley, C. Kollath, U. Schollwöck, and G. Vidal, Time-dependent density-matrix renormalization-group using adaptive effective Hilbert spaces, J. Stat. Mech. (2004) P04005.

[31] P. Schmitteckert, Nonequilibrium electron transport using the density matrix renormalization group method, Phys. Rev. B **70**, 121302(R) (2004).

[32] D. M. Kennes, V. Meden, and R. Vasseur, Universal quench dynamics of interacting quantum impurity systems, Phys. Rev. B **90**, 115101 (2014).

[33] F. H. L. Essler, S. Kehrein, S. R. Manmana, and N. J. Robinson, Quench dynamics in a model with tuneable integrability breaking, Phys. Rev. B **89**, 165104 (2014).

[34] C. Karrasch and D. Schuricht, Dynamical phase transitions after quenches in nonintegrable models, Phys. Rev. B **87**, 195104 (2013).

[35] C. Karrasch, J. E. Moore, and F. Heidrich-Meisner, Real-time and real-space spin and energy dynamics in one-dimensional spin-$\frac{1}{2}$ systems induced by local quantum quenches at finite temperatures, Phys. Rev. B **89**, 075139 (2014).

[36] P. A. McClarty, F. Krüger, T. Guidi, S. F. Parker, K. Refson, A. W. Parker, D. Prabhakaran, and R. Coldea, Topological triplon modes and bound states in a Shastry–Sutherland magnet, Nat. Phys. **13**, 736 (2017).

[37] S. Mühlbauer, D. Honecker, E. A. Périgo, F. Bergner, S. Disch, A. Heinemann, S. Erokhin, D. Berkov, C. Leighton, M. R. Eskildsen, and A. Michels, Magnetic small-angle neutron scattering, Rev. Mod. Phys. **91**, 015004 (2019).

[38] J. A. Sobota, Y. He, and Z.-X. Shen, Angle-resolved photoemission studies of quantum materials, Rev. Mod. Phys. **93**, 025006 (2021).

[39] T. Barthel, U. Schollwöck, and S. R. White, Spectral functions in one-dimensional quantum systems at finite temperature using the density matrix renormalization group, Phys. Rev. B **79**, 245101 (2009).

[40] C. Karrasch, J. H. Bardarson, and J. E. Moore, Finite-temperature dynamical density matrix renormalization group and the Drude weight of spin-1/2 chains, Phys. Rev. Lett. **108**, 227206 (2012).

[41] C. Karrasch, J. H. Bardarson, and J. E. Moore, Reducing the numerical effort of finite-temperature density matrix renormalization group calculations, New J. Phys. **15**, 083031 (2013).

[42] T. Barthel, Precise evaluation of thermal response functions by optimized density matrix renormalization group schemes, New J. Phys. **15**, 073010 (2013).

[43] A. C. Tiegel, S. R. Manmana, T. Pruschke, and A. Honecker, Matrix product state formulation of frequency-space dynamics at finite temperatures, Phys. Rev. B **90**, 060406(R) (2014).

[44] D. Jansen, J. Bonča, and F. Heidrich-Meisner, Finite-temperature optical conductivity with density-matrix renormalization group methods for the Holstein polaron and bipolaron with dispersive phonons, Phys. Rev. B **106**, 155129 (2022).

[45] T. Rakovszky, C. W. von Keyserlingk, and F. Pollmann, Dissipation-assisted operator evolution method for capturing hydrodynamic transport, Phys. Rev. B **105**, 075131 (2022).

[46] J. Sirker and A. Klümper, Real-time dynamics at finite temperature by the density-matrix renormalization group: A path-integral approach, Phys. Rev. B **71**, 241101(R) (2005).

[47] J. Kokalj and P. Prelovšek, Finite-temperature dynamics with the density-matrix renormalization group method, Phys. Rev. B **80**, 205117 (2009).

[48] H. Suwa and S. Todo, Generalized moment method for gap estimation and quantum Monte Carlo level spectroscopy, Phys. Rev. Lett. **115**, 080601 (2015).
[49] M. B. Hastings, An area law for one-dimensional quantum systems, J. Stat. Mech. (2007) P08024.
[50] M. M. Wolf, F. Verstraete, M. B. Hastings, and J. I. Cirac, Area laws in quantum systems: Mutual information and correlations, Phys. Rev. Lett. **100**, 070502 (2008).
[51] G. Krilov, E. Sim, and B. J. Berne, Quantum time correlation functions from complex time Monte Carlo simulations: A maximum entropy approach, J. Chem. Phys. **114**, 1075 (2001).
[52] X. Cao, Y. Lu, E. M. Stoudenmire, and O. Parcollet, Dynamical correlation functions from complex time evolution, Phys. Rev. B **109**, 235110 (2024).
[53] M. Grundner, P. Westhoff, F. B. Kugler, O. Parcollet, and U. Schollwöck, Complex time evolution in tensor networks and time-dependent Green's functions, Phys. Rev. B **109**, 155124 (2024).
[54] J. Haegeman, J. I. Cirac, T. J. Osborne, I. Pižorn, H. Verschelde, and F. Verstraete, Time-dependent variational principle for quantum lattices, Phys. Rev. Lett. **107**, 070601 (2011).
[55] J. Haegeman, C. Lubich, I. Oseledets, B. Vandereycken, and F. Verstraete, Unifying time evolution and optimization with matrix product states, Phys. Rev. B **94**, 165116 (2016).
[56] Z. Wang, P. McClarty, D. Dankova, A. Honecker, and A. Wietek, companion paper, Anomalous thermal broadening in the Shastry-Sutherland model and $SrCu_2(BO_3)_2$, Phys. Rev. B **113**, L041104 (2026).
[57] B. S. Shastry and B. Sutherland, Exact ground state of a quantum mechanical antiferromagnet, Physica B+C **108**, 1069 (1981).
[58] S. Miyahara and K. Ueda, Theory of the orthogonal dimer Heisenberg spin model for $SrCu_2(BO_3)_2$, J. Phys.: Condens. Matter **15**, R327 (2003).
[59] H. Kageyama, M. Nishi, N. Aso, K. Onizuka, T. Yosihama, K. Nukui, K. Kodama, K. Kakurai, and Y. Ueda, Direct evidence for the localized single-triplet excitations and the dispersive multitriplet excitations in $SrCu_2(BO_3)_2$, Phys. Rev. Lett. **84**, 5876 (2000).
[60] B. D. Gaulin, S. H. Lee, S. Haravifard, J. P. Castellan, A. J. Berlinsky, H. A. Dabkowska, Y. Qiu, and J. R. D. Copley, High-resolution study of spin excitations in the singlet ground state of $SrCu_2(BO_3)_2$, Phys. Rev. Lett. **93**, 267202 (2004).
[61] M. E. Zayed, Ch. Rüegg, Th. Strässle, U. Stuhr, B. Roessli, M. Ay, J. Mesot, P. Link, E. Pomjakushina, M. Stingaciu, K. Conder, and H. M. Rønnow, Correlated decay of triplet excitations in the Shastry-Sutherland compound $SrCu_2(BO_3)_2$, Phys. Rev. Lett. **113**, 067201 (2014).
[62] S. Miyahara and K. Ueda, Exact dimer ground state of the two dimensional Heisenberg spin system $SrCu_2(BO_3)_2$, Phys. Rev. Lett. **82**, 3701 (1999).
[63] H. Kageyama, K. Yoshimura, R. Stern, N. V. Mushnikov, K. Onizuka, M. Kato, K. Kosuge, C. P. Slichter, T. Goto, and Y. Ueda, Exact dimer ground state and quantized magnetization plateaus in the two-dimensional spin system $SrCu_2(BO_3)_2$, Phys. Rev. Lett. **82**, 3168 (1999).
[64] S. Miyahara and K. Ueda, Thermodynamic properties of three-dimensional orthogonal dimer model for $SrCu_2(B0_3)_2$, J. Phys. Soc. Jpn. Suppl. B **69**, 72 (2000).
[65] A. Wietek, P. Corboz, S. Wessel, B. Normand, F. Mila, and A. Honecker, Thermodynamic properties of the Shastry-Sutherland model throughout the dimer-product phase, Phys. Rev. Res. **1**, 033038 (2019).
[66] P. Lemmens, M. Grove, M. Fischer, G. Güntherodt, V. N. Kotov, H. Kageyama, K. Onizuka, and Y. Ueda, Collective singlet excitations and evolution of Raman spectral weights in the 2D spin dimer compound $SrCu_2(BO_3)_2$, Phys. Rev. Lett. **85**, 2605 (2000).
[67] D. Wulferding, Y. Choi, S. Lee, M. A. Prosnikov, Y. Gallais, P. Lemmens, C. Zhong, H. Kageyama, and K.-Y. Choi, Thermally populated versus field-induced triplon bound states in the Shastry-Sutherland lattice $SrCu_2(BO_3)_2$, npj Quantum Mater. **6**, 102 (2021).
[68] S. Paeckel, T. Köhler, A. Swoboda, S. R. Manmana, U. Schollwöck, and C. Hubig, Time-evolution methods for matrix-product states, Ann. Phys. **411**, 167998 (2019).
[69] M. P. Zaletel, R. S. K. Mong, C. Karrasch, J. E. Moore, and F. Pollmann, Time-evolving a matrix product state with long-ranged interactions, Phys. Rev. B **91**, 165112 (2015).
[70] G. Vidal, Efficient classical simulation of slightly entangled quantum computations, Phys. Rev. Lett. **91**, 147902 (2003).
[71] M. Yang and S. R. White, Time-dependent variational principle with ancillary Krylov subspace, Phys. Rev. B **102**, 094315 (2020).
[72] M. Fishman, S. R. White, and E. M. Stoudenmire, The iTensor software library for tensor network calculations, SciPost Phys. Codebases 4 (2022).
[73] M. Yang, M. Fishman, S. R. White, and E. M. Stoudenmire, Itensortdvp, 2023, https://github.com/ITensor/ITensorTDVP.jl.
[74] K. M. M. Prabhu, *Window Functions and Their Applications in Signal Processing* (CRC Press, Boca Raton, FL, 2018).
[75] R. N. Silver, D. S. Sivia, and J. E. Gubernatis, Maximum-entropy method for analytic continuation of quantum Monte Carlo data, Phys. Rev. B **41**, 2380 (1990).
[76] A. W. Sandvik, Stochastic method for analytic continuation of quantum Monte Carlo data, Phys. Rev. B **57**, 10287 (1998).
[77] K. S. D. Beach, Identifying the maximum entropy method as a special limit of stochastic analytic continuation, arXiv:cond-mat/0403055.
[78] H. Shao and A. W. Sandvik, Progress on stochastic analytic continuation of quantum Monte Carlo data, Phys. Rep. **1003**, 1 (2023).
[79] D. P. Landau, K. K. Mon, and H.-B. Schüttler, Computer simulation studies in condensed-matter physics: An introduction, in *Computer Simulation Studies in Condensed-Matter Physics V*, edited by D. P. Landau, K. K. Mon, and H.-B. Schüttler (Springer, Berlin, 1993), pp. 1–2.
[80] K. Vafayi and O. Gunnarsson, Analytical continuation of spectral data from imaginary time axis to real frequency axis using statistical sampling, Phys. Rev. B **76**, 035115 (2007).
[81] S. Fuchs, T. Pruschke, and M. Jarrell, Analytic continuation of quantum Monte Carlo data by stochastic analytical inference, Phys. Rev. E **81**, 056701 (2010).
[82] A. W. Sandvik, Constrained sampling method for analytic continuation, Phys. Rev. E **94**, 063308 (2016).
[83] J. Fei, C.-N. Yeh, and E. Gull, Nevanlinna analytical continuation, Phys. Rev. Lett. **126**, 056402 (2021).

[84] S. R. White and I. Affleck, Spectral function for the $S = 1$ Heisenberg antiferromagetic chain, Phys. Rev. B **77**, 134437 (2008).

[85] F. A. Wolf, J. A. Justiniano, I. P. McCulloch, and U. Schollwöck, Spectral functions and time evolution from the Chebyshev recursion, Phys. Rev. B **91**, 115144 (2015).

[86] Y. Tian and S. R. White, Matrix product state recursion methods for computing spectral functions of strongly correlated quantum systems, Phys. Rev. B **103**, 125142 (2021).

[87] A. Wietek, L. Staszewski, M. Ulaga, P. L. Ebert, H. Karlsson, S. Sarkar, H. Shackleton, A. Sinha, and R. D. Soares, XDiag: Exact diagonalization for quantum many-body systems, arXiv:2505.02901.